

Deblending the MIGHTEE-COSMOS survey with XID+: The resolved radio source counts to $S_{1.4} \approx 5\mu\text{Jy}$

Eliab Malefahlo^{*1,2}, Matt J. Jarvis^{3,2}, Mario G. Santos^{2,4}, Catherine Cress¹, Daniel J.B. Smith⁵, Catherine Hale^{3,6}, José Afonso^{7,8}, Imogen H. Whittam^{3,2}, Mattia Vaccari^{9,10,11}, Ian Heywood^{12,3,13}, Shuowen Jin^{14,15}, Fangxia An^{16,9}

¹UNISA Centre for Astrophysics and Space Sciences, College of Science, Engineering and Technology, University of South Africa, Cnr Christian de Wet Rd and Pioneer Avenue, Florida Park, 1709 Roodepoort, South Africa

²Department of Physics & Astronomy, University of the Western Cape, Private Bag X17, Bellville, Cape Town, 7535, South Africa

³Astrophysics, Department of Physics, University of Oxford, Keble Road, Oxford, OX1 3RH, UK

⁴South African Radio Astronomy Observatory (SARAO), 2 Fir Street, Observatory, Cape Town, 7925, South Africa

⁵Centre for Astrophysics Research, University of Hertfordshire, Hatfield, Herts, AL10 9AB, UK

⁶Institute for Astronomy, University of Edinburgh, Royal Observatory Edinburgh, Blackford Hill, Edinburgh, EH9 3HJ, UK

⁷Instituto de Astrofísica e Ciências do Espaço, Universidade de Lisboa, OAL, Tapada da Ajuda, PT1349-018 Lisbon, Portugal

⁸Departamento de Física, Faculdade de Ciências, Universidade de Lisboa, Edifício C8, Campo Grande, PT1749-016 Lisbon

⁹Inter-University Institute for Data Intensive Astronomy, Department of Astronomy, University of Cape Town, 7701 Rondebosch, Cape Town, South Africa

¹⁰Department of Astronomy, University of Cape Town, Rondebosch, Cape Town, 7701, South Africa

¹¹INAF - Istituto di Radioastronomia, via Gobetti 101, 40129 Bologna, Italy

¹²SKA Organization, Jodrell Bank, Lower Whittington, Macclesfield, SK11 9FT, UK

¹³Centre for Radio Astronomy Techniques and Technologies, Department of Physics and Electronics, Rhodes University, PO Box 94, Makhanda, 6140, South Africa

¹⁴Cosmic Dawn Center (DAWN), Denmark

¹⁵DTU Space, Technical University of Denmark, Elektrovej 327, 2800 Kgs. Lyngby, Denmark

¹⁶Yunnan Observatories, Chinese Academy of Sciences, Kunming 650216, People's Republic of China

Accepted XXX. Received YYY; in original form ZZZ

ABSTRACT

Deep radio continuum surveys provide fundamental constraints on galaxy evolution, but source confusion limits sensitivity to the faintest sources. We present a complete framework for producing high-fidelity deblended radio catalogs from the confused MIGHTEE maps using the probabilistic deblending framework XID+ and prior positions from deep multi-wavelength data in the COSMOS field. To assess performance, we construct MIGHTEE-like simulations based on the Tiered Radio Extragalactic Continuum Simulation (T-RECS) radio source population, ensuring a realistic distribution of star-forming galaxies and active galactic nuclei (AGN) for validation. Through these simulations, we show that prior catalog purity is the dominant factor controlling deblending accuracy: a high-purity prior, containing only sources with a high likelihood of radio detection, recovers accurate flux densities and reproduces input source counts down to $\sim 3\sigma$ (where σ = thermal noise). On the other hand, a complete prior overestimates the source counts due to spurious detections. Our optimal strategy combines the high-purity prior with a mask that removes sources detected above $50\mu\text{Jy}$. Applied to the $\sim 1.3\text{ deg}^2$ area of the MIGHTEE-COSMOS field defined by overlapping multi-wavelength data, this procedure yields a deblended catalog of 89,562 sources. The derived 1.4 GHz source counts agree with independent P(D) analyses and indicate that we resolve the radio background to $\sim 4.8\mu\text{Jy}$. We also define a recommended high-fidelity sample of 20,757 sources, based on detection significance, flux density, and goodness-of-fit, which provides reliable flux densities for individual sources in the confusion-limited regime.

Key words: methods: data analysis – methods: statistical – galaxies: statistics – radio continuum: galaxies – surveys

1 INTRODUCTION

The bright radio sky, at Giga-Hertz frequencies and flux densities above a few millijanskys (mJy), is dominated by a powerful population of radio-loud Active Galactic Nuclei (AGN; e.g., [Kellermann et al. 1989](#); [Best & Heckman 2012](#); [Hardcastle & Croston 2020](#);

[Whittam et al. 2022](#)). In these sources, the observed emission is predominantly non-thermal synchrotron radiation, produced as relativistic electrons, accelerated within powerful jets launched by central supermassive black holes (e.g., [Blandford & Rees 1974](#); [Blandford & Königl 1979](#)). The statistical distribution of extragalactic sources is an important tool in cosmology, quantified by the differential source counts (dN/dS), which measure the number of sources per unit solid angle as a function of flux density. At these bright, mJy-to-Jy flux

* eliabmalefahlo3@gmail.com

densities, where radio-loud AGN dominate, the normalized counts are relatively flat due to the rarity of these luminous AGN, whose sky density is very low (e.g., Condon 1984). However, below a few mJy, they exhibit a well-established upturn, a clear signature that the source population is evolving and was significantly more numerous (e.g., Condon 1984; Windhorst et al. 1985). This upturn marks a shift in the nature of the dominant radio source population.

The emerging population that dominates the faint sub-mJy and μ Jy radio sky is now understood to be composed of two main classes of object: star-forming galaxies (SFGs) and radio-faint AGN (e.g., Jarvis & Rawlings 2004; Wilman et al. 2008; de Zotti et al. 2010; White et al. 2015, 2017; Padovani 2016; Smolčić et al. 2017). In SFGs, the radio emission at Giga-Hertz frequencies originates from processes linked to massive stars: it is dominated by non-thermal synchrotron radiation from cosmic-ray electrons accelerated in supernova remnants (the endpoints of massive stellar evolution), and a smaller contribution from thermal free-free emission from HII regions, which are clouds of interstellar gas ionized by the intense ultraviolet radiation from young, massive stars (Condon 1992; Bell 2003; Murphy et al. 2011; Kennicutt & Evans 2012). Because these processes are a direct consequence of recent massive star formation, the radio luminosity serves as a well-established tracer of the star formation rate (SFR, Condon 1992). Furthermore, because radio waves are unaffected by the dust that obscures optical and ultraviolet light, these observations provide one of the least biased measures of the cosmic star formation history, an important quantity for galaxy evolution studies (Karim et al. 2011; Jarvis et al. 2015; Novak et al. 2017; Ocran et al. 2020; Matthews et al. 2021b; Malefahlo et al. 2022; Wang et al. 2024a; Matthews et al. 2024).

The origin of radio emission in the radio-quiet AGN population, is a subject of ongoing debate. Defined as AGN that lack the powerful, large-scale relativistic jets characteristic of their radio-loud counterparts, their radio emission is orders of magnitude weaker. One theory argues that the emission, while weak, is still intrinsically linked to AGN activity, such as small-scale jets, coronal emission from the accretion disk, or outflows and winds (White et al. 2015, 2017; Hwang et al. 2018; Rankine et al. 2021; Wang et al. 2025). An alternative theory is that this emission is not directly related to the AGN but is instead dominated by star formation in the host galaxy (Kimball et al. 2011; Condon et al. 2013; Bonzini et al. 2013; Gürkan et al. 2015; Malefahlo et al. 2020). The current consensus suggests that both processes likely contribute, but their relative importance as a function of key parameters like black hole accretion rate, stellar mass, and redshift remains a key open question in galaxy evolution (e.g. Bonfield et al. 2011; Hickox et al. 2014; Panessa et al. 2019; Macfarlane et al. 2021; Yue et al. 2024; Kondapally et al. 2025).

The radio emission originating from star-formation processes is empirically found to correlate tightly with the infrared luminosity of galaxies, a relationship first discovered in the far-infrared (FIR; Helou et al. 1985; Yun et al. 2001) and now commonly referred to as the total infrared–radio correlation (IRRC; e.g., Bell 2003). This near-linear correlation holds over several orders of magnitude in luminosity and is known to extend to high redshifts, although its precise evolution with cosmic time remains an active area of research (e.g., Jarvis et al. 2010; Magnelli et al. 2015; Read et al. 2018; Delhaize et al. 2017; Delvecchio et al. 2021). Given the strong correlation between far-infrared emission and the star-formation rate (SFR), this leads to the radio-SFR relation (e.g. Yun et al. 2001; Bell 2003; Gürkan et al. 2018; Smith et al. 2021) and the potential to study star-formation in the highest redshift galaxies (e.g. Whittam et al. 2025). There is a growing body of evidence that demonstrates that it is not only pure star-forming galaxies that follow this relation;

the host galaxies of most low-luminosity and radio-quiet AGN are also observed to lie on or very near the IRRC (e.g. Moloko et al. 2025).

The current generation of radio telescopes has now reached the sensitivity, resolution and survey speed needed to probe the μ Jy sky in detail. Key instruments include the MeerKAT telescope in South Africa (Jonas 2009; Booth et al. 2009), the Australian SKA Pathfinder (ASKAP; Johnston et al. 2008), and the Low-Frequency Array (LOFAR; van Haarlem et al. 2013). These are enhanced by upgraded arrays like the Giant Metrewave Radio Telescope (uGMRT Gupta et al. 2017), with the future Square Kilometre Array Observatory (SKAO; Braun et al. 2015) and the Next Generation Very Large Array (ngVLA; Murphy et al. 2018) set to push sensitivity even further. With their ability to combine sub- μ Jy sensitivity with arcsecond resolution over wide fields, these facilities are designed specifically to address key questions in galaxy evolution: to build a complete census of the cosmic star formation history, disentangle the faint SFG and radio-faint AGN populations, and investigate the faint-end slope of the radio source counts.

Despite these instrumental advances, deep surveys run into the instrumental confusion: the surface density of faint sources becomes so high that individual objects overlap/blend due to the telescope’s beam, making direct detection and photometry unreliable (Condon 1974; Zwart et al. 2015). There are two strategies that have been developed to push beyond confusion. The first is the probability of deflection or P(D) analysis, which can recover the underlying source counts but does not provide individual source flux densities (Scheuer 1957; Condon 1974; Condon et al. 2012; Vernstrom et al. 2014; Matthews et al. 2021a). The second approach is prior-driven deblending, which uses high-resolution ancillary data to model and partition the confused maps, predominantly for submillimetre and far-infrared data (Tibshirani 1996; Zou 2006; Magnelli et al. 2010; Béthermin et al. 2010; Roseboom et al. 2010; Chapin et al. 2011; Lee et al. 2013; Wang et al. 2014; Hurley et al. 2017; Jin et al. 2018; Wang et al. 2024b). The prior-driven approach has multiple methods, from image-plane model fitting like ‘super-deblending’ (Liu et al. 2018; Jin et al. 2018) to probabilistic Bayesian frameworks like XID+ (Hurley et al. 2017), which samples the full posterior probability distribution of flux densities. However, the success of these probabilistic frameworks is highly sensitive to the construction of the prior lists.

In this paper, we develop and validate a complete framework based on this probabilistic approach to produce a deblended radio source catalog from the confused survey maps of the MeerKAT International GHz Tiered Extragalactic Exploration (MIGHTEE) survey (Jarvis et al. 2016; Heywood et al. 2021). MIGHTEE is a large survey project using the MeerKAT telescope to map deep extragalactic fields, with the first data release (DR1; Hale et al. 2025) providing the data for this work. We use realistic simulations to optimize our methodology before applying this validated strategy to the MIGHTEE observations of the Cosmic Evolution Survey (COSMOS; Scoville et al. 2007) field. In Section 2, we describe the MIGHTEE radio data and the ancillary multi-wavelength catalogs used to construct our prior lists. Section 3 provides a brief overview of the XID+ deblending framework. In Section 4, we present the analysis of realistic simulations used to validate and optimize our deblending strategy. In Section 5, we apply this optimized strategy to the MIGHTEE-COSMOS field, presenting the final deblended flux catalog and radio source counts. Finally, we summarize our key findings and conclusions in Section 6. Throughout this paper, we assume a flat Λ CDM cosmology with $H_0 = 70 \text{ km s}^{-1} \text{ Mpc}^{-1}$, $\Omega_M = 0.3$, and $\Omega_\Lambda = 0.7$. Furthermore, we

define the radio spectral index (α) by the power-law relation between flux density (S_ν) and frequency (ν), given by $S_\nu \propto \nu^\alpha$.

2 DATA

This section details the primary radio data, the ancillary multi-wavelength catalogs, the star-galaxy classification process, and the final definition of the master galaxy sample used for subsequent analysis.

2.1 MIGHTEE DR1 Radio Data

We use radio data from the first MIGHTEE data release, DR1 (Hale et al. 2025). This release includes deep imaging over 20 deg^2 of the COSMOS, XMM-LSS, and CDFS fields. For this work, we focus specifically on the MIGHTEE-COSMOS field, which covers a total area of 4.2 deg^2 . The DR1 data for this field were produced from 22 individual pointings, totaling 139.6 hours of on-target time at L-band ($\sim 1.2\text{--}1.3 \text{ GHz}$). The final mosaicked images are released at two resolutions: a lower resolution ($\sim 8.9 \text{ arcsec}$) prioritizing sensitivity and a higher resolution ($\sim 5.2 \text{ arcsec}$). The thermal noise is $\sim 1.6 \mu\text{Jy/beam}$ (lower resolution) and $\sim 2.2 \mu\text{Jy/beam}$ (higher resolution), with a median measured total noise across the mosaic of $\sim 3.5 \mu\text{Jy/beam}$ (Hale et al. 2025). We adopt two distinct noise symbols throughout: σ for the thermal noise and σ_{Tot} for the total noise, which includes confusion noise σ_{conf} . The depth and area of these maps make them rich with faint sources, leading to source confusion that motivates this work. We apply the deblending technique to the deeper low-resolution data, which suffers more from confusion (Heywood et al. 2021).

2.2 Ancillary Multi-wavelength Data

The probabilistic deblending performed in this work requires an input prior list of potential source positions. We construct our master source list using the deep multi-wavelength catalog presented by Varadaraj et al. (2023), which builds upon the data compilation of Adams et al. (2021). This catalog is built upon the UltraVISTA DR4 near-infrared (NIR) data (McCracken et al. 2012), providing deep Y , J , H , and K_s band photometry. This is complemented by optical coverage from the Hyper Suprime-Cam (HSC) Subaru Strategic Program PDR3 (Aihara et al. 2022), as well as data from the Canada-France-Hawaii Telescope (CFHT; Gwyn 2012) and *Spitzer*/IRAC 3.6 and $4.5 \mu\text{m}$ photometry (Fazio et al. 2004; Mauduit et al. 2012).

To obtain the necessary physical properties for our prior construction, we use the COSMOS2020 photometric catalog (Weaver et al. 2022). This is a comprehensive, panchromatic photometric catalog covering the COSMOS field, updated from the COSMOS2015 release (Laigle et al. 2016). It includes new, deep imaging data from several key surveys: U-band data from the CLAUDS survey (Sawicki et al. 2019), g , r , i , z , y -band data from the HSC Subaru Strategic Program PDR2 (Aihara et al. 2019), Y , J , H , K_s -band data from the UltraVISTA DR4 survey (McCracken et al. 2012), and updated *Spitzer*/IRAC data from the Cosmic Dawn Survey (Euclid Collaboration et al. 2022). Source detection was performed on a deep, χ^2 $izYJHKs$ detection image. We use the "Farmer" catalog, which was generated using the Tractor software, where the catalog is limited to the UltraVISTA footprint (Weaver et al. 2022).

From this catalog, we use the photometric redshifts and inferred total infrared luminosities ($L_{\text{IR}} = \text{rest-frame } 8\text{--}1000 \mu\text{m}$ luminosity) derived using the EAZY code (Brammer et al. 2008). This L_{IR} value

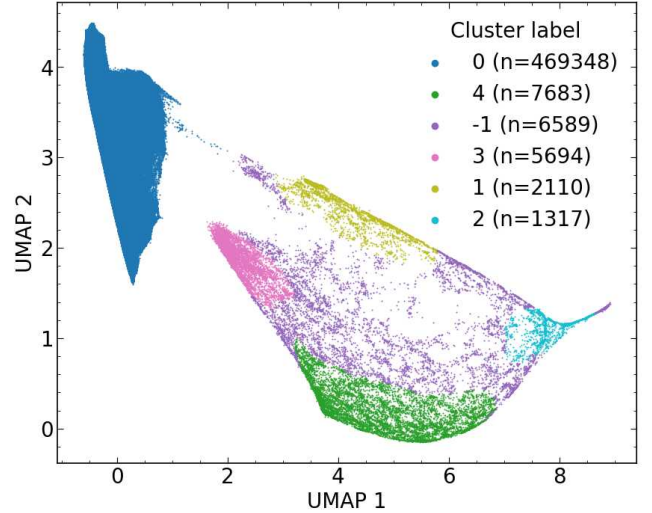


Figure 1. A projection of sources onto the first two dimensions from the Uniform Manifold Approximation and Projection (UMAP) algorithm. These UMAP axes are abstract dimensions derived from the input photometry. Colors represent classifications by HDBSCAN. The main population of galaxies is shown in blue (Cluster 0). The other colors represent distinct populations of stellar sources identified by the clustering algorithm.

is an inferred quantity derived from SED fitting based on the principle of energy balance. Specifically, this calculation is based on the method implemented in the EAZY code, which uses Flexible Stellar Population Synthesis (FSPS) templates (Conroy et al. 2009) to model the starlight and estimate the energy absorbed by dust. This absorbed energy is then assumed to be re-radiated in the FIR, following the spectral templates of Magdis et al. (2012).

The catalog includes a FLAG_COMBINED column, which identifies sources within a clean area of 1.278 deg^2 with full HSC, VISTA, and *Spitzer*/IRAC coverage and removes sources affected by bright stars or artifacts. We use this flag in the final stage of our analysis (Section 5) when constructing our final prior list. For the prior list construction, we cross-match our master catalog with the full Farmer dataset (964,506 sources) using a search radius of 0.3 arcsec . This results in a matched sample of 650,148 sources, which serves as the basis for our star-galaxy classification.

2.3 Star-Galaxy Classification

A significant challenge in constructing a prior list from deep optical/IR catalogs is the presence of stellar sources. Since most stars are not detectable radio sources (e.g. Driessen et al. 2024; Egbo et al. 2025), their inclusion in the prior list would introduce a population of non-emitting sources. This could cause the deblending algorithm to assign radio flux incorrectly from nearby galaxies to these stellar positions, thereby contaminating the measurements of genuine radio galaxies. Therefore, a reliable method for star-galaxy separation is an important preliminary step.

2.3.1 Methodology

Our star-galaxy classification process begins with the 650,148 sources matched between our master catalog and COSMOS2020. We use the HSC PDR3 photometry for classification because its improved depth enables more reliable morphological separation compared to earlier releases. We apply two selection criteria to ensure

that we use robust photometry. First, we select sources with a signal-to-noise ratio in the K_s -band of $\text{SNR} > 5$, reducing the sample to 506,136 sources.

To classify these sources, we use a two-stage unsupervised machine learning process, following [Cook et al. \(2024b\)](#). Unsupervised learning has the advantage of not being biased by a given training set, which is critical for faint source populations where complete and representative training data are unavailable (see [Fotopoulou 2024](#), for a review). First, we construct a high-dimensional feature space from the photometric data. We use magnitudes from the optical HSC survey and the near-infrared from VISTA to generate 28 color combinations. These colors, combined with the 8 original magnitude measurements (g, r, i, z, Y, J, H, K_s), serve as 36 features for each source. While some color features are mathematically redundant, we include all of them, as dimensionality reduction techniques like Uniform Manifold Approximation and Projection (UMAP; [McInnes et al. 2018](#)) effectively extracts the most important underlying information from complete feature sets ([Cook et al. 2024b](#)). Furthermore, we verified that a reduced set of independent features (e.g., a single magnitude band plus $n-1$ independent colors) produced a consistent classification, confirming the robustness of the approach. This high-dimensional feature space provides a more robust basis for distinguishing between stellar and galactic populations than is possible in any single two-dimensional parameter space (e.g. [Strateva et al. 2001](#); [Hewett et al. 2006](#)).

Before applying the machine learning algorithms, the feature set is first cleaned by removing sources with incomplete photometry, which yields a working sample of 492,741 sources. This feature set is then scaled using the `StandardScaler` package from `scikit-learn` ([Pedregosa et al. 2011](#)). This process applies a standard Z-score transformation, rescaling each feature to have a mean of zero and a standard deviation of one, which ensures that all features contribute equally to the analysis.

The first stage of the process applies the UMAP algorithm to this feature space ([McInnes et al. 2018](#)). UMAP is a non-linear dimensionality reduction technique that reduces the 36-dimensional feature space to a 10-dimensional embedding¹ while preserving the essential topological structure of the data ([Becht et al. 2019](#)). Its ability to capture the complex, non-linear relationships inherent in multi-band photometric data makes it a superior choice to simpler linear methods like Principal Component Analysis (PCA; [Jolliffe & Cadima 2016](#)). Furthermore, UMAP has been shown to be more scalable and better at preserving the global structure of the data, crucial for separating the main star and galaxy clusters, than comparable techniques ([McInnes et al. 2018](#)).

The second stage applies the Hierarchical Density-Based Spatial Clustering of Applications with Noise (HDBSCAN) algorithm ([McInnes et al. 2017](#)) to identify distinct clusters in the UMAP-reduced space. HDBSCAN is a density-based algorithm that can find clusters of varying shapes and densities without requiring the number of clusters to be specified beforehand, making it effective at isolating the primary stellar and galactic populations (e.g. [Logan & Fotopoulou 2020](#); [Fotopoulou 2024](#)).

¹ These 10 output dimensions are abstract representations; each is a complex, non-linear combination of the original 36 photometric features and does not correspond directly to any single physical property like a specific color or magnitude.

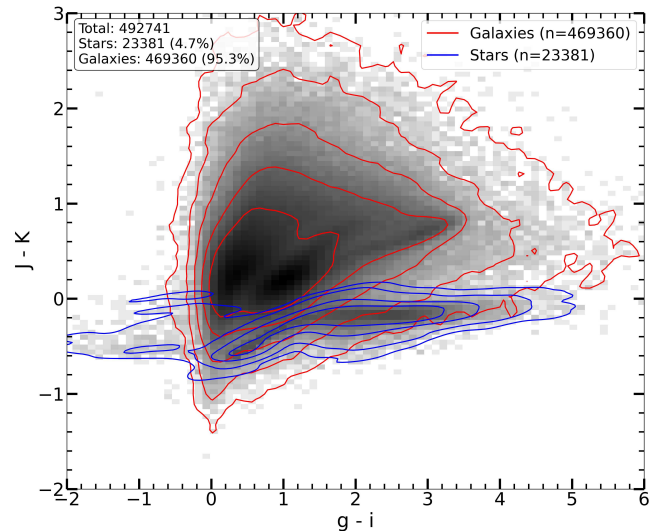


Figure 2. $J - K$ vs. $g - i$ color-color diagram for the 492,741 sources. The underlying greyscale density map shows the distribution of the full sample. The overlaid contours trace the density of sources classified as galaxies (red) and stars (blue), illustrating the separation achieved by the high-dimensional analysis.

Table 1. Star-galaxy classification breakdown for the VISTA + HSC PDR3 dataset.

Classification	Number of Sources	Percentage
Galaxies	469,360	95.3 per cent
Stars	23,381	4.7 per cent
Final Total	492,741	100 per cent

2.3.2 Application

We applied this methodology to the filtered sample of 492,741 sources derived from the cross-matched dataset. The process successfully separates the sources, yielding a catalog of 469,360 high-confidence galaxies (95.3 per cent) and 23,381 stars (4.7 per cent), as detailed in [Table 1](#). The resulting UMAP projection, which clearly shows the distinct clusters, is presented in [Figure 1](#). The classification is visualized on the traditional $J - K$ vs. $g - i$ color-color diagram (e.g., [Jarvis et al. 2013](#)) in [Figure 2](#). In this two-dimensional projection, while the bulk of the populations lie on distinct loci, the contours reveal a region of degeneracy where stars and galaxies overlap. Traditional methods, which rely on defining a fixed boundary or simple curves relative to the stellar locus (e.g., [Jarvis et al. 2013](#)), inevitably suffer from contamination or incompleteness in this overlapping regime. However, our machine learning approach uses the full high-dimensional feature space to resolve these degeneracies and successfully disentangles stars and galaxies that are indistinguishable in the $J - K$ vs. $g - i$ plane alone.

2.4 The Galaxy Sample and prior list construction

Following star-galaxy classification, we define a galaxy sample from which deblending priors are constructed. We select all galaxies from our filtered sample that have a total infrared luminosity (L_{IR}) estimate from the COSMOS2020 catalog. This results in a galaxy list of 331,442 galaxies within the region of overlapping deep multi-

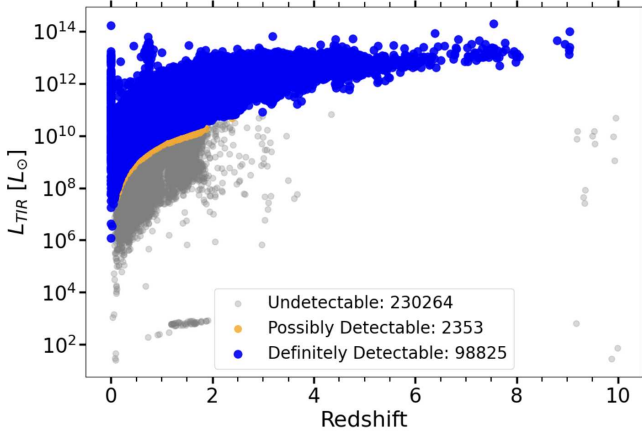


Figure 3. The distribution of the galaxy sample in the total infrared luminosity (L_{IR}) versus redshift plane. Sources are classified based on their predicted 1.4 GHz flux density relative to the MIGHTEE sensitivity limit. Blue dots represent sources classified as ‘Definitely Detectable’ ($S_{\text{pred}} > 1 \mu\text{Jy}$), orange dots indicate ‘Possibly Detectable’ sources (where the upper L_{IR} uncertainty bound implies $S_{\text{pred}} > 1 \mu\text{Jy}$), and grey dots show ‘Undetectable’ sources.

wavelength coverage. This sample forms the basis for all subsequent prior list construction.

Constructing a prior list presents a trade-off between completeness and purity. An inclusive prior ensures that all potential radio-emitting galaxies are considered, but at the risk of including a large number of undetectable radio sources. As demonstrated by Hurley et al. (2017), an excess of such priors can degrade the flux measurements of genuine detections by incorrectly partitioning the map’s flux density. To investigate this trade-off and determine the optimal strategy for MIGHTEE, we construct two distinct prior lists from our galaxy sample, each designed to test a different deblending philosophy.

The first prior list is designed to be as inclusive as possible. It incorporates all 331,442 sources from our galaxy sample that have an L_{IR} measurement. We supplement this list with 4,754 sources detected above 3σ in the VLA-COSMOS 3 GHz survey (Smolčić et al. 2017), as extracted by Jin et al. (2018), specifically adding those that do not have counterparts in our optical/NIR sample. This results in a candidate list of 336,196 unique sources. This Comprehensive L_{IR} Prior represents a compromise, aiming for high completeness by including any source with evidence of significant star formation or AGN activity (via L_{IR}) without being as exhaustive as including all $\sim 470,000$ galaxies in the master sample.

The second prior list is designed to be an optimized list containing only sources with a high probability of being detectable in the radio. In this context, we define ‘detectable’ not as a strict $> 5\sigma$, but as a source having a flux density sufficient to be statistically measurable. This Radio-Likely Prior is designed as a high-purity sample, containing sources with a high probability of detection while excluding those expected to be undetectable. This provides a cleaner and more effective input for XID+. The construction is a two-step process.

First, we predict the 1.4 GHz radio flux density for each of the 331,442 galaxies in our galaxy sample based on their estimated infrared luminosity, using the well-established IRRc (Helou et al. 1985; Condon 1992; Yun et al. 2001). The methodology is as follows:

(i) The rest-frame 1.4 GHz radio luminosity ($L_{1.4}$) is calculated from the total infrared luminosity (L_{IR}) using the linear correla-

tion from Cook et al. (2024a), given by $\log_{10}(L_{\text{IR}}/L_{\odot}) = 11.170 + 0.921 \log_{10}(L_{1.4}/5 \times 10^{22} \text{ W Hz}^{-1})$.

(ii) This radio luminosity is converted to an expected observed flux density ($S_{1.4}$) using the source’s redshift (z) and corresponding luminosity distance (D_L), including a k-correction of the form $(1+z)^{1-\alpha}$. We assume a spectral index $\alpha = 0.7$, a typical value for the synchrotron-dominated emission of star-forming galaxies at these frequencies (Condon 1992).

(iii) Sources are then classified based on a comparison to the MIGHTEE map sensitivity. Those with a predicted flux density above our threshold (of $1 \mu\text{Jy}$) are flagged as ‘Definitely Detectable’. To account for uncertainties, we also identify sources that fall below this threshold but whose predicted flux density based on the upper error bound of their L_{IR} exceeds it; these are flagged as ‘Possibly Detectable’.

The results of this prediction step are shown in Figure 3. As expected, the 98,825 sources predicted to be ‘Definitely Detectable’ occupy the high- L_{IR} regime across all redshifts, with the 2,353 ‘Possibly Detectable’ sources forming a boundary region where detection is plausible given L_{IR} uncertainties.

Second, this core list of likely radio-bright sources is supplemented with the same VLA radio sources used for the comprehensive prior to ensure completeness for known radio-emitting sources. This results in a candidate list of 106,164 unique galaxies for the Radio-Likely Prior.

3 XID+ PROBABILISTIC DEBLENDING TECHNIQUE

Having established a prior list of source positions from ancillary data, we now address the challenge of measuring their flux densities in the confused MIGHTEE radio maps. We use the probabilistic deblending framework XID+ (Hurley et al. 2017) to perform this task. Even among prior-driven deblending approaches, many rely on maximum-likelihood estimation to assign flux (e.g., FASTPHOT, Béthermin et al. 2010). While computationally efficient, these approaches can struggle in highly confused regimes, often incorrectly assigning the total flux density of a blend to a single source and failing to provide robust uncertainty estimates (e.g. Roseboom et al. 2010; Wang et al. 2014).

XID+ overcomes these limitations by adopting a fully probabilistic Bayesian framework (Hurley et al. 2017). Instead of seeking a single best-fit solution, XID+ explores the entire parameter space to map out the full posterior probability distribution for the flux of every source (Hurley et al. 2017). This approach has several advantages. First, it provides uncertainty quantification by naturally capturing the credible intervals and degeneracies that arise when multiple sources are close together. Second, the joint posterior reveals covariance between sources, quantifying how the flux density estimate of one source is correlated with its neighbors. Third, the Bayesian framework correctly models the behavior of sources at or below the noise level.

The core assumption of XID+ is that the observed map data, d , can be modelled as a linear combination of the flux densities, S , of a known set of N_s prior sources, each treated as a point source convolved with the instrument’s Point Spread Function (PSF), plus a background (B) and noise component (n). For this work, we use the Gaussian restoring beam from the low-resolution MIGHTEE data. This noise is modelled as a Gaussian that accounts for both thermal noise and confusion noise arising from the blending of faint unresolved sources (e.g. Condon 1974). For a map flattened into a

vector of M pixels, this can be expressed as:

$$d = PS + n + B, \quad (1)$$

where: P is the $M \times N_s$ pointing matrix, which represents the PSF response of each prior source. It is constructed by placing a model of the instrument PSF at the sky position of each source in the prior list.

The Bayesian paradigm seeks the posterior probability of the fluxes given the data, $p(S|d)$, which is given by Bayes' theorem:

$$p(S|d) \propto p(d|S) \times p(S). \quad (2)$$

Here, $p(d|S)$ is the likelihood of observing the data given a set of fluxes, and $p(S)$ is the prior probability distribution of the fluxes. The likelihood is modelled as a multivariate Gaussian distribution based on the noise properties of the map. The standard XID+ framework calculates the total variance by adding the thermal variance (from a user-provided map) and a fitted confusion variance in quadrature ($\sigma_{\text{Tot}}^2 = \sigma^2 + \sigma_{\text{conf}}^2$). However, a pure thermal noise map was not available for the MIGHTEE DR1 data products; instead, a total noise RMS map, which already accounts for both effects, was provided (Hale et al. 2025). This means the standard likelihood calculation within XID+ could not be used without modification.

For the deblending performed in this work, we use a simple, uninformative (flat) prior for the flux of each source, typically bounded between 0 and a sufficiently high value, to avoid biasing the resulting measurements towards any pre-conceived model (Hurley et al. 2017; Wang et al. 2024b). The role of the ancillary data is therefore to define an optimal and pure list of source positions, rather than to inform the flux priors directly.

Solving for the full posterior distribution in Equation 2 is a high-dimensional problem that is computationally intractable to solve analytically. XID+ addresses this by using the probabilistic programming language Stan (Carpenter et al. 2017). Specifically, it uses the No-U-Turn Sampler (NUTS, Hoffman & Gelman 2014), to efficiently draw samples from the high-dimensional posterior distribution. To accommodate the MIGHTEE DR1 noise map, we modified the XID+ Stan code to use the pre-computed total variance from the DR1 RMS map at each pixel ($\sigma_{\text{Tot}}^2 = \sigma_{\text{DR1_RMS}}^2$) directly in the likelihood calculation. While this means we do not derive a separate confusion noise component, it ensures the deblending is performed using the most accurate, position-dependent noise estimate available. An important parameter governing the sampler's exploration is `max_treedepth`, which controls the complexity of the integration paths, with a default value of 10. Testing on real MIGHTEE data in Section 5.3 shows that increasing this to 15 was required for convergence. Following the recommendation of Hurley et al. (2017), we run four independent MCMC chains to ensure convergence.

Fitting the whole map at once is computationally unfeasible, so the analysis is partitioned into small tiles using the HEALPix framework (Górski et al. 2005), each ~ 3.4 arcmin across (HEALPix order 10). However, to ensure an accurate flux measurement for sources within one of these small tiles, the deblending fit must account for flux spilling in from bright sources in the surrounding area. Therefore, the fit is performed on a much larger 'fitting' tile, ~ 27.5 arcmin across (HEALPix order 7), which fully encompasses the smaller results tile. Once the fit on the larger tile is complete, only the results for sources within the central small tile are retained. The primary output for each source within a successfully fitted tile is a chain of samples from its posterior distribution. The point estimates for the deblended flux densities for each source are taken as the median (50th percentile) of its posterior distribution for each source. The

final catalog is produced by repeating this process for all tiles across the map and combining the results.

4 DEBLENDING VALIDATION WITH SIMULATIONS

While XID+ has been extensively and successfully applied to confused FIR and sub-millimetre data from instruments like *Herschel* and SCUBA-2 (e.g., Hurley et al. 2017; Pearson et al. 2017; Shirley et al. 2021; Wang et al. 2024b), its application to deep radio continuum data is less established. Radio surveys present a unique set of challenges, including more complex source morphologies (e.g., core-jet-lobe structures in AGNs; Mingo et al. 2019; Hardcastle & Croston 2020), which violates the point-source assumption of XID+ (see Section 3).

Therefore, before applying XID+ to the MIGHTEE data, it is essential to conduct a thorough validation using realistic simulations. These simulations provide a known ground truth, allowing us to test the performance of XID+ under radio-specific conditions and to identify the optimal configuration for our deblending strategy.

4.1 The Simulation Framework

Our simulations generate realistic radio sky models that capture the morphological diversity of galaxies and the basic properties of MIGHTEE. The framework, adapted from Harrison et al. (2020) and implemented in a custom Python script, uses the `galsim` (Rowe et al. 2015) software package to draw galaxy models into a simulated map. The properties of the source population are drawn from the Tiered Radio Extragalactic Continuum Simulation (T-RECS) catalog (Bonaldi et al. 2019, 2023).

The modeling of galaxy morphology is tailored to the source type to achieve a high degree of realism:

- **SFGs:** These are modeled using Sersic profiles (Sérsic 1963). The Sersic index (n) is set based on the galaxy's optical classification (e.g., $n = 1$ for disk-like, $n = 4$ for bulge-like), while the scale radius, flux, and orientation are taken from the T-RECS catalog values.
- **AGNs:** AGN modeling depends on their radio classification. Compact AGNs (FSRQs, BL Lacs) are modeled as single, compact Gaussian profiles.

The more complex Steep-Spectrum AGNs (SS-AGNs), corresponding to Fanaroff-Riley Class I (FRI) and II (FR II) sources (Fanaroff & Riley 1974), are modeled with a multi-component structure. The total flux is distributed among a core, jets, and lobes, with the fractional contribution of each component depending on the R_s parameter, defined as the ratio between the total projected source size and the projected distance between the two bright hot spots, from the T-RECS catalog, which distinguishes between core- and lobe-dominated structures. The overall source size is similarly apportioned between a central region and outer structures, with the relative extent of the jets and lobes also governed by the R_s parameter to model the brighter, more extended jets of FRIs and the dominant lobes of FR IIs.

To mimic the asymmetric structures observed in real radio surveys (e.g., Laing & Bridle 2002), we implement a bending model where each side of the AGN is assigned randomized parameters for an angular offset, a shear, and a positional shift. The distributions from which these random values are drawn are different for FRI and FR II sources, allowing for the larger, more distorted morphologies characteristic of FRI jets. The final model components are then: a

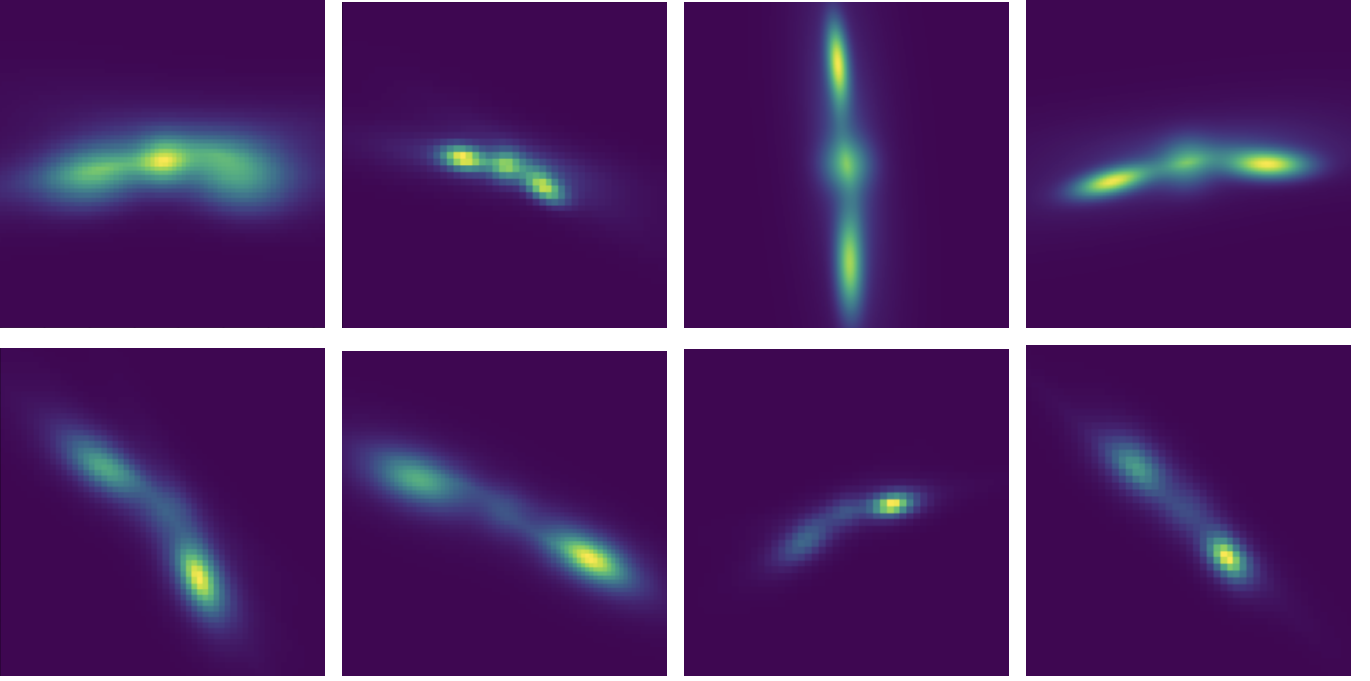


Figure 4. Examples of the complex, multi-component AGN morphologies generated by our simulation pipeline. The top row displays four Fanaroff-Riley Type I (FRI) sources, modeled with bent jets. The bottom row displays four Fanaroff-Riley Type II (FR II) sources, featuring distinct lobes and hotspots. All images are 50×50 pixels in size, with a pixel scale of 1.1 arcsec.

compact Gaussian core; composite jets made of a central, straight exponential profile and two outer bent exponential profiles; and lobes modeled as either diffuse Gaussians (for FRIs) or sharper Moffat profiles to represent hotspots (for FR IIs), reflecting the different termination shocks in the two classes (e.g., [Hardcastle & Croston 2020](#)). Each component’s final position and orientation are determined by the bending model, ensuring a morphologically diverse and realistic AGN population. Figure 4 demonstrates the morphological complexity incorporated into our simulations. The top row displays FRI sources, characterized by their core-dominated, bent-jet structures, while the bottom row shows FR II sources with distinct hotspots and lobes. While these parametric models do not capture the full physical evolution inherent in hydrodynamic simulations (e.g., [Giri et al. 2024](#)), they successfully reproduce the structural diversity, such as bent jets and asymmetric lobes, required to challenge the deblending algorithm. This level of realism is sufficient to quantify the impact of non-point-source emission on XID+ flux recovery.

The primary validation tests were conducted on a simulated map configured to match the MIGHTEE low-resolution data, with a pixel scale of 1.1 arcsec and where the source models are convolved with a Gaussian PSF of 8.6 arcsec FWHM. The simulation includes sources from the T-RECS catalog down to a flux limit of $0.5 \mu\text{Jy}$, sources fainter than this limit contribute negligibly to the final map statistics given the target noise level. For these tests, we added uniform Gaussian noise with a σ of $1.3 \mu\text{Jy}/\text{beam}$, a value representative of the thermal noise in the deepest parts of the MIGHTEE fields ([Hale et al. 2025](#)).

4.2 Validating the Simulation

Before using the simulation to test our deblending approach, we must first validate that the simulation itself is a reliable representation of the radio sky.

For a quantitative test, we apply a blind source-finding algorithm Python Blob Detection and Source Finder (PyBDSF; [Mohan & Rafferty 2015](#)) to the simulated map. We use a multi-stage process similar to that for the official MIGHTEE DR1 catalogs ([Hale et al. 2025](#)) as well as for the ELAIS-N1 field from the LOFAR Two-metre Sky Survey Deep Fields Data Release 2 ([Shimwell et al. 2025](#)). This approach is necessary for deeply confused fields like those studied here as a single-pass source-finding run is insufficient because the presence of numerous faint, undetected sources elevates the measured total noise (σ_{Tot}). This artificially high noise level can prevent the detection of other faint sources that would otherwise meet the detection threshold.

The multi-stage approach consists of three main steps. For all three steps, we run PyBDSF using its default parameters, which include a $3\sigma_{\text{Tot}}$ island threshold and a $5\sigma_{\text{Tot}}$ detection threshold. First, an initial pass of PyBDSF is run on the original map. This initial run generates both a catalog of the sources and a corresponding residual map. Secondly, we run PyBDSF on the residual map and we obtain a more accurate map of the background total noise. In the final step, this improved noise map is used as input for a second PyBDSF run on the original. This procedure allows the source-finder to identify faint sources, leading to a more complete and accurate source catalog.

The results from this process are shown in Figure 5, which we use to validate our simulation. At bright flux densities ($S_{1.4} > 100 \mu\text{Jy}$), the recovered flux densities are in good agreement with the input values, lying tightly along the one-to-one correlation line. This holds true for all source types, including the morphologically complex Extended AGNs and Extended SFGs. However, at flux densities below $S_{1.4} \sim 100 \mu\text{Jy}$, and particularly for the dominant population of Compact SFGs, a systematic overestimation of flux or “flux boosting” begins to emerge and becomes increasingly severe towards lower flux densities. This is a well-documented effect in deep radio surveys (e.g., [Jauncey 1968](#); [Zwart et al. 2015](#) and references within), and its impact on

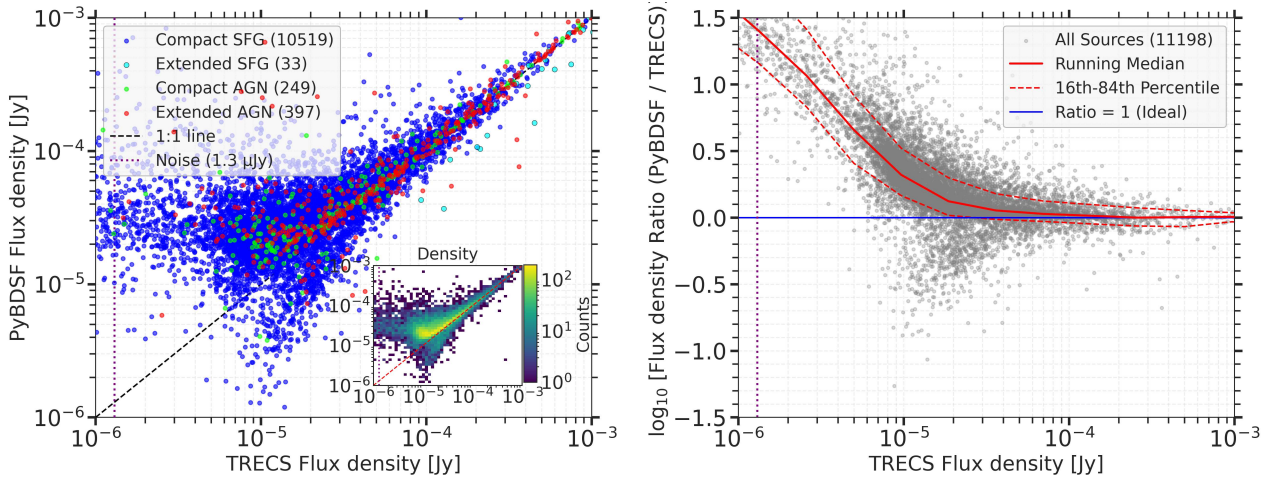


Figure 5. Left: Comparison of input T-RECS catalog flux densities versus flux densities recovered by a multi-stage PyBDSF source-finding process on the simulated map. Sources are colored by type: Compact SFGs (blue), Extended SFGs (cyan), Compact AGNs (green), and Extended AGNs (red). The dashed black line indicates a perfect 1:1 correlation. Right: The log-ratio of recovered PyBDSF-to-true flux versus true flux for all sources (grey points). The solid red line is the running median of this ratio, with the dashed red lines showing the 16th-84th percentile range. The solid blue line indicates a perfect recovery ratio of 1.

the MIGHTEE DR1 source counts was characterized and corrected for using simulations by Hale et al. (2025). The right-hand panel quantifies this trend: the running median of the flux ratio, which is close to unity for bright sources, gradually climbs, reaching a factor of three (0.5 dex) at the faintest flux levels ($S_{1.4} \sim 10\mu\text{Jy}$).

The analysis shows that even after the multi-stage process mitigates noise-related biases, we still have a systematic overestimation of flux at faint levels. This is due to source confusion. When multiple physically distinct sources lie closer than the telescope’s resolution, any source-finder will tend to group their emission into a single detection, incorrectly assigning their combined flux to one position. This demonstrates that while our multi-stage PyBDSF approach is valid for finding sources, it is not well-suited to providing accurate faint-source flux measurements in a confused map. For this task, a deblending algorithm like XID+ is required for probing the faint radio sky.

4.3 Determining the Optimal Deblending Strategy

We now use the simulation as a testbed to determine the most effective configuration for implementing XID+. We focus on three parameters: the mask type used for masking of bright, complex sources, the level threshold of the masking, and the composition of the prior input list.

4.3.1 Masking Strategy: Threshold and Type

The XID+ framework assumes point-like sources, an assumption that breaks down for the very bright, resolved, or morphologically complex objects that blind source-finders detect most easily. These sources must be masked to prevent them from corrupting the flux density estimates of neighbouring faint sources.

Our masking is based on PyBDSF Gaussian models. We first select bright sources with a total or peak flux density above a certain threshold. We then construct a 2D model of the source using the fitted parameters (flux density, major axis, minor axis, position angle) from PyBDSF for each of these bright sources. The individual source mask is generated by identifying all pixels within this model that exceed a $1\sigma_{\text{Tot}}$ level relative to the total noise of the map.

We determine the optimal flux density thresholds for masking by examining the performance of the blind source-finder (PyBDSF) in our simulations (Figure 5). We define two thresholds based on the regimes where blind extraction becomes unreliable due to confusion:

- The $S > 50\mu\text{Jy}$ mask: This mask removes all sources with flux densities $S_{1.4} > 50\mu\text{Jy}$ ($\log_{10}(S) > -4.3$). As shown in the right panel of Figure 5 (cyan line), this nominal threshold corresponds approximately to the onset of systematic flux boosting, where the PyBDSF recovered flux begins to systematically deviate from the input values. By masking sources brighter than this limit, we remove the population that is reasonably well-recovered by blind source finding, creating a “cleaner” map for XID+ to deblend the remaining faint, confused population where blind extraction fails.
- The $S > 250\mu\text{Jy}$ mask: This mask removes only sources with $S_{1.4} > 250\mu\text{Jy}$ ($\log_{10}(S) > -3.6$). This threshold corresponds to the bright regime where the PyBDSF recovery is unbiased (ratio ≈ 1) and the scatter is minimal. This strategy preserves a larger area and a greater number of intermediate-brightness sources for deblending, providing a test of XID+ in a more challenging environment with higher source density.

In addition to the flux density threshold, we test the impact of the catalog type used to generate the mask. PyBDSF’s process involves first identifying ‘islands’ of contiguous emission above a given threshold, and then fitting one or more Gaussian components to model the flux within each island. From this, it produces two primary catalogs: a Gaussian component list (GAUL), which contains the parameters of every individual Gaussian component fitted to the emission islands, and a source list (SRL), which groups related Gaussian components into what the algorithm interprets as single astrophysical objects. These catalogs are known to trace different aspects of the radio source population, particularly for bright and extended sources. By testing these different configurations, we can determine which masking approach yields the most reliable deblended flux densities for the remaining faint source population.

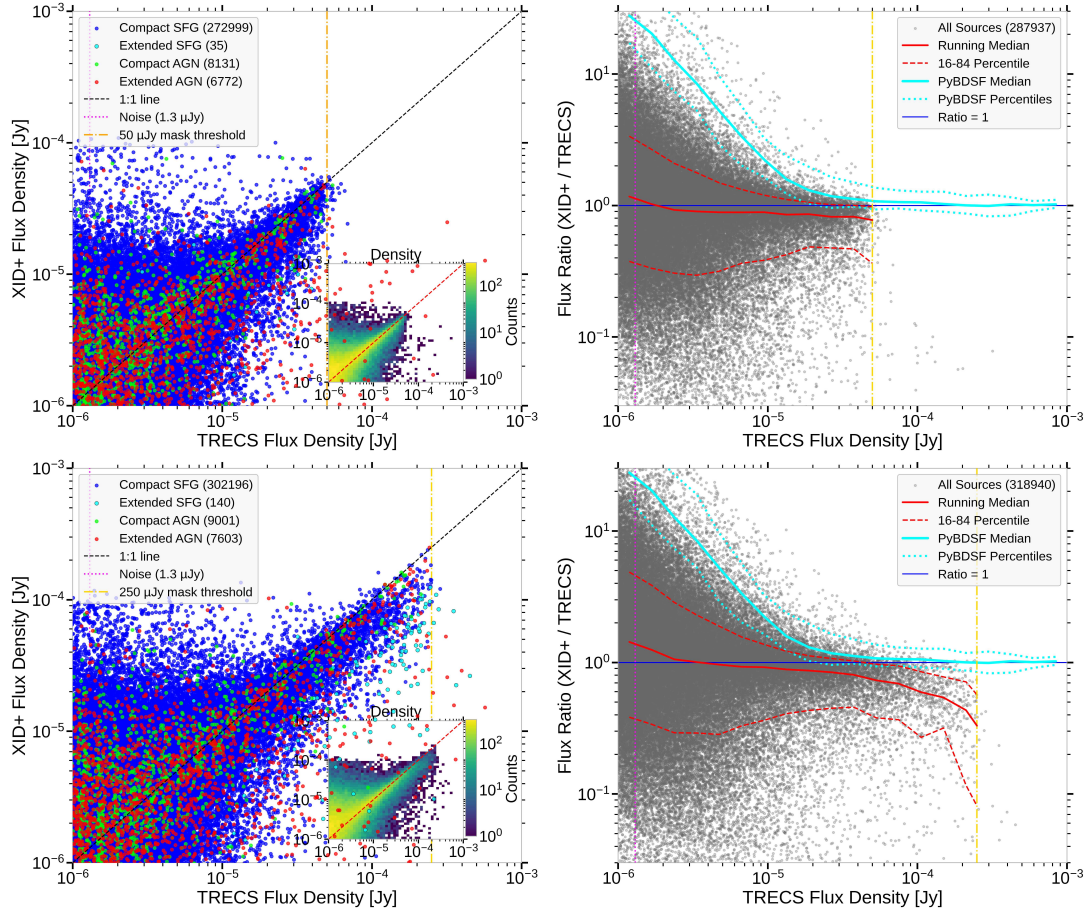


Figure 6. XID+ debinding performance using the **full T-RECS prior** with masks derived from the PyBDSF SRL catalog. Each plot consists of two panels. The left panel shows the debinded flux from XID+ versus the true input flux from the T-RECS simulation, with sources colored by type: Compact SFG (blue), Extended SFG (cyan), Compact AGN (green), and Extended AGN (red). The dashed black line indicates a perfect 1:1 recovery, and the inset shows a 2D density histogram of the points. The right panel shows the log-ratio of debinded-to-true flux versus true flux for all sources (grey points). The solid red line is the running median of this ratio, with the dashed red lines showing the 16th-84th percentile range. The solid cyan line shows the running median from PyBDSF, with dotted cyan lines showing its percentile range. The solid blue line indicates a perfect recovery ratio of 1. Top plot: masking all sources brighter than $50 \mu\text{Jy}$ using the SRL catalog. Bottom Plot: masking all sources brighter than $250 \mu\text{Jy}$ using the SRL catalog.

4.3.2 Prior list Selection

The performance of XID+ is dependent on the quality of the prior catalog. We test two scenarios:

- **Full T-RECS Prior:** A complete prior that is analogous to using the unfiltered optical/NIR catalog for the real data. It contains the true positions of all sources from the simulation that fall within the unmasked regions.
- **Radio-Likely Prior:** An optimized prior, the simulation analog of the Radio-Likely Prior from Section 2.4, constructed by selecting all sources from the full T-RECS catalog with an intrinsic flux greater than $1 \mu\text{Jy}$. This tests how XID+ performs with a high-purity but necessarily incomplete prior list.

The number of sources in each of these sub-samples for the different masking configurations is detailed in Table 2.

4.4 Deblending Performance and Flux Recovery

We assess the performance of the debinding strategies by examining the accuracy (bias, via the running median of the flux ratio)

Table 2. Number of T-RECS sources in the simulated field under different masking and prior selection criteria.

Simulation configuration	Number of Prior Sources	
	Full Prior	Radio-Likely Prior
Total Sources in Field (no masked)	329,178	80,574
Using PyBDSF GAUL-based Masking		
Remaining after $50 \mu\text{Jy}$ Masking	279,598	65,738
Remaining after $250 \mu\text{Jy}$ Masking	317,338	77,562
Using PyBDSF SRL-based Masking		
Remaining after $50 \mu\text{Jy}$ Masking	288,014	67,307
Remaining after $250 \mu\text{Jy}$ Masking	319,017	77,673

and the precision (scatter, via the 16th-84th percentile range) of the debinded flux densities relative to the true T-RECS values.

4.4.1 Improvement Over Blind Source Finding

PyBDSF suffers from strong flux boosting towards faint flux density (Figure 5). All XID+ debinding strategies show a marked improvement for the faint source population. They all maintain a running me-

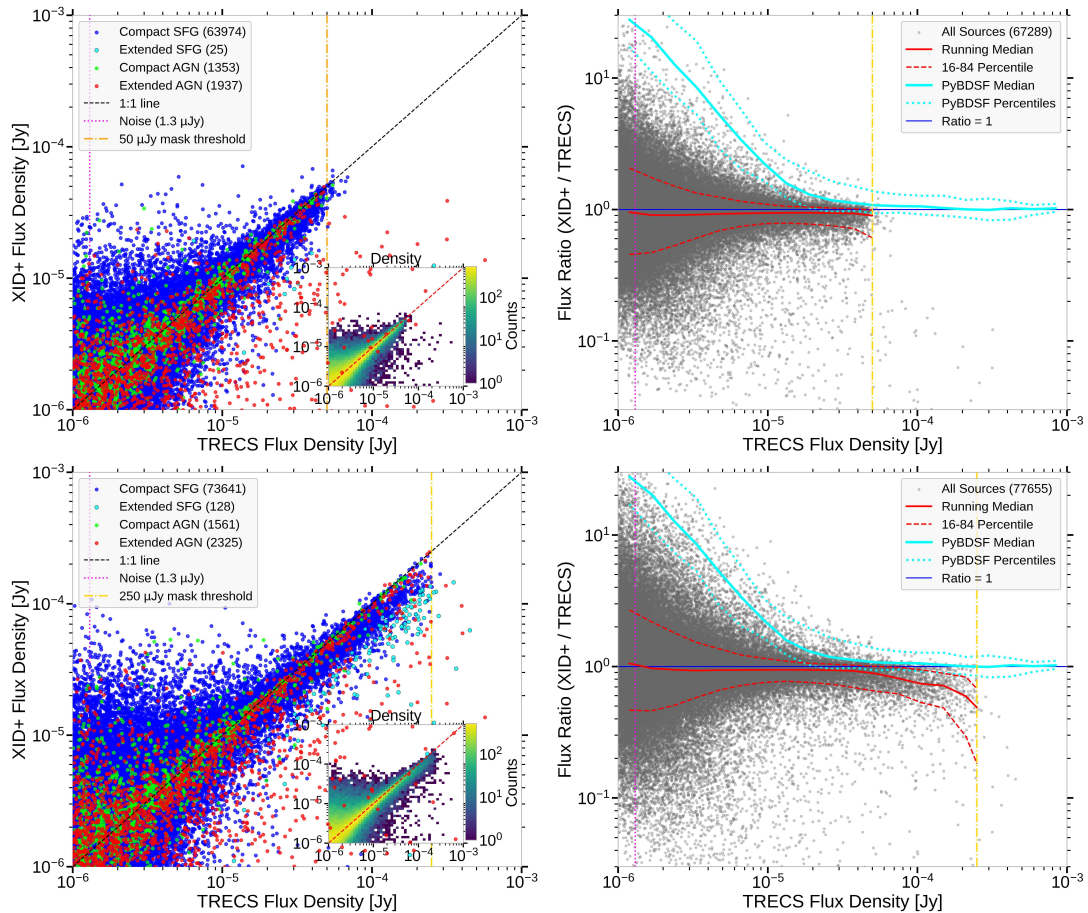


Figure 7. XID+ deblending performance using the optimal but incomplete Radio-Likely Prior with masks derived from the PyBDSF SRL catalog. The panels and symbols are the same as in Figure 6. Top: Performance when masking sources brighter than $50 \mu\text{Jy}$ using the GAUL catalog. Bottom: Performance when masking sources brighter than $250 \mu\text{Jy}$ using the GAUL catalog. For the sources included in the prior, the flux recovery is excellent in both cases, but the $50 \mu\text{Jy}$ mask yields a tighter correlation with lower scatter, producing the most reliable flux measurements.

dian flux ratio much closer to zero across the deblended flux range, with typical deviations of less than 0.05 dex for faint sources. Even the least optimal strategy, therefore, successfully addresses the primary bias inherent in blind source-finding methods. However, while the accuracy (bias) is consistently improved, the precision (scatter) of the deblended flux densities varies significantly among the different strategies.

4.4.2 The Impact of Prior Catalog Quality

The choice of prior list is the dominant factor affecting the precision of the deblended flux densities. When using the Full Prior, which contains all sources from the T-RECS simulation in the unmasked area, the deblending precision is relatively poor. As shown in Figure 6 (top; $50 \mu\text{Jy}$ mask), the 16th–84th percentile range of the flux ratio widens from approximately 0.4 dex at $30 \mu\text{Jy}$ to 0.8 dex at $3 \mu\text{Jy}$. This indicates that a typical $3 \mu\text{Jy}$ source has an uncertainty of almost an order of magnitude.

This high scatter is a direct consequence of over-deblending, where the algorithm incorrectly partitions flux among the dense list of faint priors. Furthermore, the errors are not symmetric; the running median of the flux ratio is consistently closer to the 84th percentile than the 16th, revealing a systematic skew where individual sources are more likely to have their flux overestimated than underestimated.

Although this strategy successfully removes the large positive flux-boosting bias seen in PyBDSF (Figure 5), it introduces a large, asymmetric error in its place.

The performance improves significantly with the Radio-Likely Prior as shown in Figures 7. For the same $50 \mu\text{Jy}$ mask and $30 \mu\text{Jy}$ flux level, the 16th–84th percentile range narrows dramatically to just ± 0.15 dex. This factor of three improvement in precision demonstrates that a high-purity, albeit incomplete, prior is important for obtaining reliable individual flux measurements. We note a small but systematic negative bias of -0.02 dex (a ~ 4.5 per cent underestimation) that is stable across the flux range, as well as a mild skew (~ 0.05 dex median offset) emerging at fainter flux densities. By reducing the number of faint, ambiguous priors, the algorithm converges on more stable and better-constrained solutions.

4.4.3 The Role of the Masking Threshold

While the prior list governs the overall precision, the choice of masking threshold affects both the precision and the accuracy of the deblended flux densities, particularly for sources near the mask limit. For both prior catalogs, masking sources $> 50 \mu\text{Jy}$ ($50 \mu\text{Jy}$ mask) consistently produces better results compared to the $250 \mu\text{Jy}$ mask.

When using the optimal Radio-Likely Prior, switching from a $50 \mu\text{Jy}$ mask (Figure 7, top) to a $250 \mu\text{Jy}$ mask (Figure 7, bottom)

degrades precision. The 16th–84th percentile range at 30 μ Jy widens from 0.15 dex to 0.25 dex. This confirms that creating a cleaner deblending environment by removing moderately bright sources improves the precision of the remaining faint-source measurements.

The masking threshold also affects the accuracy for sources near the mask limit. When using the 250 μ Jy mask, the median flux ratio decreases sharply above 60 μ Jy, reaching -0.15 dex (~ 30 per cent deficit) near the masking threshold (Fig. 7, bottom). Extended AGNs and SFGs are particularly affected as XID+’s point-source assumption fails for their complex emission. The 50 μ Jy mask eliminates this bias by excluding such sources. The 250 μ Jy mask also degrades faint-source recovery. The 50 μ Jy mask is the best choice, as it yields both higher precision for faint sources and avoids the flux underestimation bias for bright, complex sources.

4.4.4 Masking type: SRL vs. GAUL

We also tested whether the catalog type used to generate the mask, SRL versus the GAUL, impacts the deblended flux densities. The choice between these two is not trivial, as they are known to behave differently at both the bright and faint ends of the source population. As shown by Hale et al. (2022), the SRL catalog is more physically meaningful for bright, resolved radio galaxies, while the GAUL catalog can be a better tracer of the underlying source population in the confusion-dominated faint regime.

Given these known differences, it is important to test whether the choice of masking catalog (SRL vs. GAUL) type impacts the final deblended flux densities. A direct comparison of the results shows that the deblending performance is qualitatively and quantitatively very similar regardless of the masking catalog used. The 50 μ Jy threshold consistently produces lower scatter and more reliable flux densities, whether it is based on the SRL or GAUL list. The reason is that the two catalogs diverge only for the very brightest, multi-component sources, which are already removed by the 50 μ Jy mask.

4.4.5 The optimal strategy

The Radio-Likely prior provides substantially improved precision for individual flux density estimates, while the 50 μ Jy mask reduces contamination from bright, complex neighbours without introducing a systematic underestimation for faint sources. Furthermore, as shown in Section 4.4.4, the choice of masking catalog (SRL vs GAUL) has a negligible impact at this threshold. We therefore adopt the combination of the Radio-Likely prior with a 50 μ Jy SRL-based mask for all subsequent validation.

4.5 Robustness Tests

Having established the optimal deblending configuration in idealized conditions, we now subject this configuration to two rigorous stress tests to evaluate its robustness against real-world observational challenges: spatially varying noise and positional uncertainties.

4.5.1 Validation with Spatially Varying Noise

To test the robustness of our strategy against realistic observational noise conditions, we apply our recommended strategy, the Radio-Likely Prior and SRL 50 μ Jy mask, to a larger simulation that incorporates a realistic, spatially varying noise similar to the MIGHTEE-COSMOS field. We generated an analytic model by modelling the primary beam of each of the 22 MIGHTEE-COSMOS

pointings as a Gaussian and summing their squared responses on a grid matching the real data (Hale et al. 2025). This creates an idealised weight map, which is then inverted to produce a theoretical RMS map ($\sigma_{\text{Tot}} \propto 1/\sqrt{\text{weight}}$).

This process reproduces some of the features of the real observations, including the lower noise in the field center where multiple pointings overlap, and higher noise at the edges. This pre-computed RMS map is then used as input for a `galsim VariableGaussianNoise` generator, which adds the appropriate level of noise to each pixel of the noiseless simulated sky (Rowe et al. 2015).

Figure 8 shows the deblended flux performance for this more realistic simulation, using our recommended 50 μ Jy mask. At first glance, the scatter plot for this large-scale simulation appears to show a significantly wider distribution of points than the uniform-noise case, with a greater number of outliers. However, a quantitative analysis of the bulk population reveals that the core performance remains excellent. The running median of the flux ratio remains stable, with the small systematic bias shifting only slightly from -0.02 dex to -0.03 dex. Similarly, the precision, as measured by the 16th–84th percentile range, widens only modestly from 0.30 dex to 0.35 dex at 30 μ Jy.

This test shows that the statistical performance of the deblending remains robust against spatially varying sensitivity; the increased number of outliers reflects the larger survey area rather than a failure of the deblending algorithm.

4.5.2 Positional Offsets

In addition to noise variations, we tested the impact of positional offsets between radio and optical/infrared hosts, which can arise from both astrometric uncertainties and genuine physical displacements such as extended jets. To assess the robustness of our strategy to such offsets, we performed a dedicated stress test in which we shifted the positions of all simulated sources using an empirical offset distribution measured from the MIGHTEE Early Science multi-wavelength catalog (Whittam et al. 2024). These offsets were derived from 6,102 sources securely matched using the likelihood ratio method, ensuring they represent the true astrometric scatter of the survey. We applied these offsets to the input catalog before re-running our adopted configuration (Radio-Likely prior, 50 μ Jy mask). This process reduced the number of successfully matched sources (within 2.5 arcsec) from 67,307 to 62,878, a loss of ~ 7 per cent, providing a realistic estimate of the catalog yield under imperfect positional assumptions.

As shown in Figure 9, at faint flux densities ($S \lesssim 4 \mu$ Jy), the recovered flux density is the most sensitive to positional uncertainties. At $\sim 1.8 \mu$ Jy, the median recovered-to-true flux ratio decreases from 0.90 in the ideal simulation to 0.80 when offsets are applied, doubling the bias. The scatter similarly increases from 0.54 dex to 0.73 dex. When comparing this to other configurations/tests, the positional offsets produce a larger scatter and bias than either the 250 μ Jy mask (0.64 dex scatter) or the spatially varying noise simulation (0.53 dex scatter). However, the performance remains superior to the Full Prior, which suffers from a scatter of ~ 0.90 dex in this regime.

At intermediate flux densities ($S \approx 10 \mu$ Jy), the effect of positional offsets is substantially weaker. The median ratio changes only slightly from 0.94 to 0.91, and the scatter remains tight, increasing from 0.15 dex to 0.18 dex. In this regime, the choice of prior remains the dominant factor governing accuracy. The simulation with positional offsets yields a precision comparable to both the 250 μ Jy mask and the spatially varying noise runs (~ 0.16 to 0.19 dex). For bright sources ($S \gtrsim 30 \mu$ Jy), the performance is nearly unchanged.

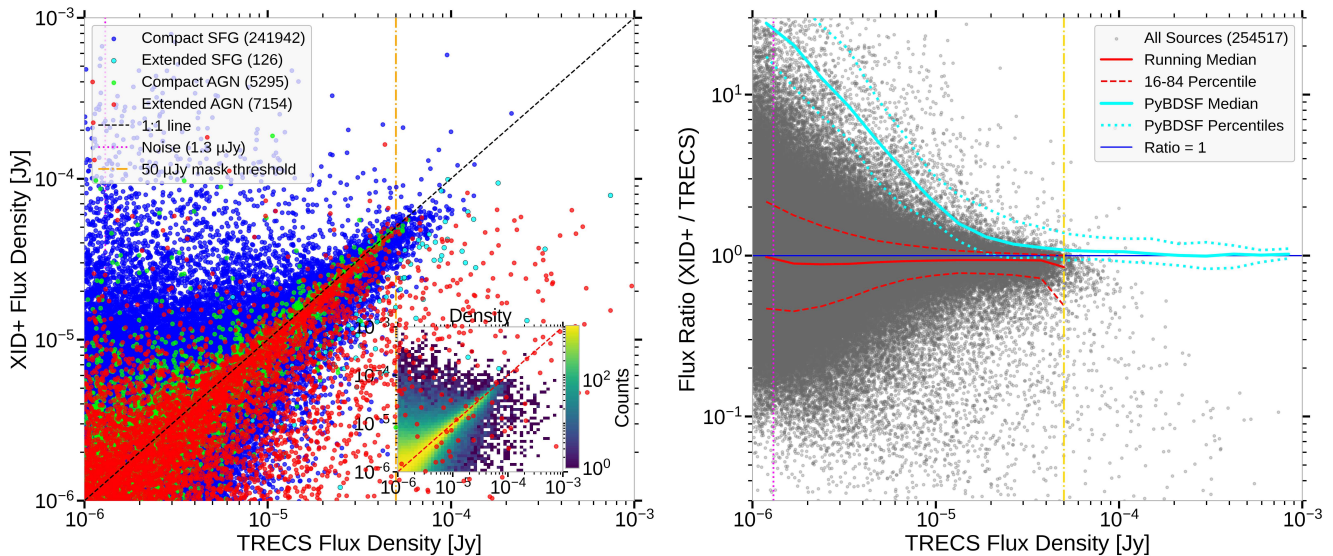


Figure 8. XID+ debinding performance on a large-scale simulation with realistic, spatially varying noise, using the Radio-Likely Prior and the $50 \mu\text{Jy}$ SRL mask. The panels and symbols are the same as in Figure 6. The flux recovery remains excellent and is highly consistent with the results from the idealized uniform-noise simulation, demonstrating the robustness of the pipeline to realistic noise conditions.

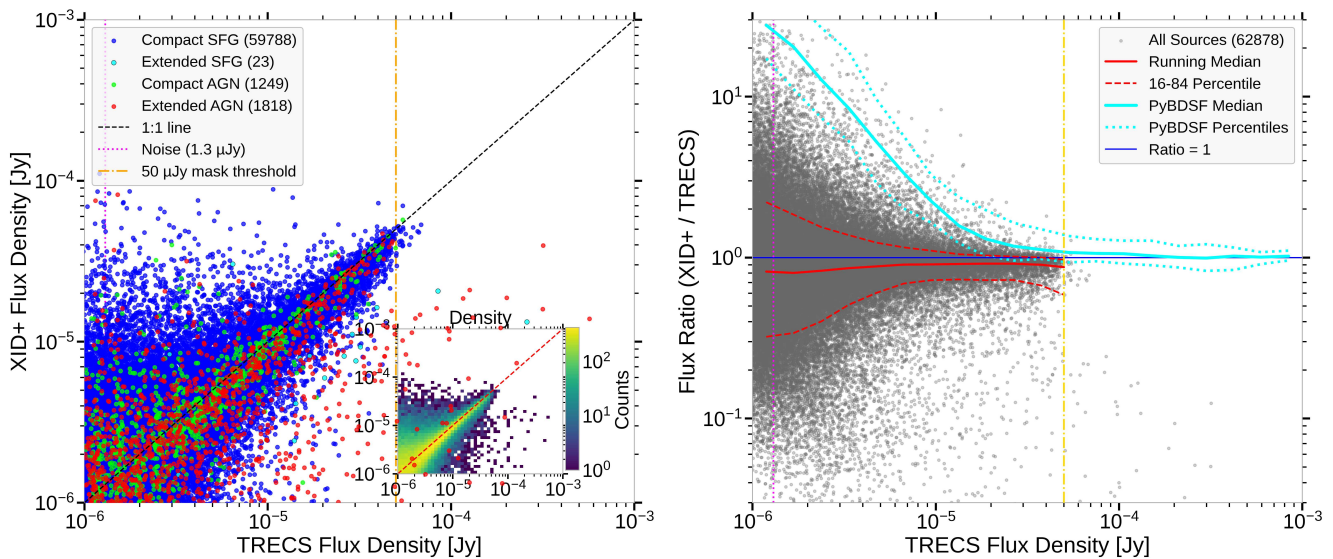


Figure 9. XID+ debinding performance using the Radio-Likely Prior and a $50 \mu\text{Jy}$ SRL mask, where the input prior positions were shifted using empirical offsets drawn from the MIGHTEE Early Science multiwavelength catalog. The panels and symbols are the same as in Figure 6.

In summary, while positional offsets represent the main source of scatter at the faintest flux densities, their relative impact decreases rapidly with increasing S/N. Although applying these shifts yields higher scatter than the idealized simulations, the performance remains better than that obtained using the full T-RECS prior. This demonstrates that the adopted Radio-Likely Prior with a $50 \mu\text{Jy}$ mask is robust to the level of positional mismatch expected in real observations, ensuring reliable flux recovery for the bulk of the source population.

4.6 The Reliability of Individual debinded flux densities

The stress tests in Section 4.5 confirm that our optimal strategy performs well under realistic noise and positional offsets. We now

examine the statistical reliability of the individual flux measurements themselves, focusing on uncertainty calibration, posterior asymmetry, detection significance, and goodness-of-fit.

4.6.1 Flux density and uncertainty recovery

An informative test of the debinding framework is to assess whether the recovered flux densities are unbiased relative to their estimated uncertainties. We construct a normalized residual distribution, shown in Figure 10, which plots the quantity (True Flux density - XID+ flux density) / (XID+ Uncertainty). Because XID+ reports asymmetric posterior intervals, we adopt a conservative, single-value uncertainty per source defined as the larger of the upper (84th - 50th percentile) and lower half-intervals (50th - 16th percentile). Using the larger

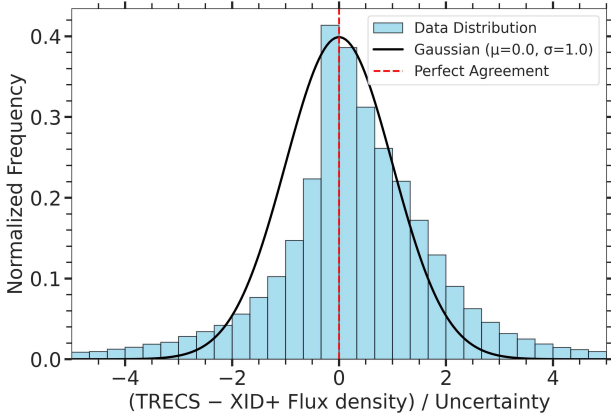


Figure 10. The normalized residual distribution for the simulated sources. The x-axis shows the difference between the true T-RECS flux and the recovered XID+ flux, divided by the XID+ uncertainty. The blue histogram shows the distribution for our data. The solid black line is a standard normal (Gaussian) distribution with a mean (μ) of 0.0 and a standard deviation (σ) of 1.0, which represents the ideal result. The red dashed line indicates the ideal mean of zero.

half-interval ensures that the significance is not overstated for skewed posteriors and makes the test conservative. For unbiased measurements with correctly calibrated uncertainties, this distribution should follow a Gaussian with mean zero and unit variance.

The observed distribution is complex. The peak is shifted slightly to the left of zero, while it also shows an excess of sources with positive residuals compared to the ideal Gaussian, particularly in the 0 to +2 range. These competing features result in a global mean for the distribution that is extremely close to zero. This demonstrates that while there are competing statistical effects on individual sources, the catalog as a whole is unbiased.

This finding is consistent with the flux ratio analysis in Section 4.4.2, which used the running median and found a small systematic underestimation of ~ 4.5 per cent. The fact that different statistical estimators (the mean of the residuals versus the median of the flux ratio) on this non-Gaussian distribution both show that any systematic bias is minor, at the few-percent level, provides strong support for the reliability of the results.

4.6.2 Individual Flux density Uncertainties

To understand the nature of the individual uncertainties, we examine the asymmetry of the posterior probability distributions, as shown in Figure 11. We quantify the shape of the posterior by the ratio of the upper uncertainty (84th - 50th percentile) to the lower uncertainty (50th - 16th percentile). A ratio of 1 indicates a symmetric, Gaussian-like posterior. For the vast majority of sources, the posterior remains symmetric (ratio ≈ 1) down to flux densities comparable to, and even slightly below, the $1.3 \mu\text{Jy}$ (1σ) noise limit. This indicates that for most sources at the noise level, the uncertainties are well-behaved. For faint sources below the noise limit, the ratio becomes $\gg 1$. This is an expected consequence of the posterior being truncated by the physical non-negativity constraint on flux density, resulting in a skewed distribution with a long tail towards higher values. Interestingly, the plot also reveals a population of sources at intermediate flux densities that exhibit highly skewed uncertainties (ratio > 2), raising questions about the reliability of these flux measurements.

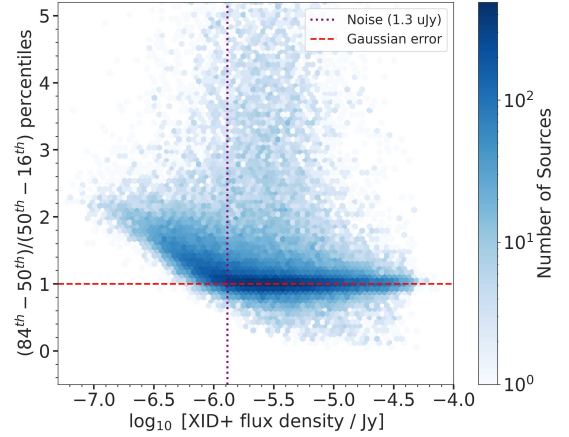


Figure 11. The asymmetry of the posterior uncertainty as a function of debled flux density for the $50 \mu\text{Jy}$ mask and Radio-Likely Prior. The y-axis shows the ratio of the upper (84th - 50th) to the lower (50th - 16th) percentile intervals. A ratio of 1 (red dashed line) indicates symmetric (Gaussian-like) posteriors. The bulk of the source population remains symmetric down to flux densities below the noise limit ($1.3 \mu\text{Jy}$, purple dotted line).

4.6.3 Assessing Detection Significance

The presence of sources with skewed or asymmetric posteriors at all flux density levels, as identified in the previous section, motivates an assessment of how posterior skewness affects detection reliability. We investigate this by examining the recovered statistical significance of each source against its true input flux density in Figure 12. We define the significance as the ratio of the median recovered flux density to its conservative uncertainty (defined in Section 4.6.1 as the maximum of the upper and lower error bounds). This ensures that we do not overestimate the significance of sources with skewed posterior distributions.

The result is a positive correlation between the true flux density and the recovered significance across the entire flux density range. The sources with skewed posteriors (orange and blue points) follow the same statistical trend as the symmetric ones (grey points); but cover a wider range of significance, which increases with decreasing flux density. This shows that a simple flux density cut is not a sufficient criterion for selecting a sample of well-constrained sources. For example, at a true flux density of $3.9 \mu\text{Jy}$ (the 3σ limit), sources can have significances ranging from less than 1 to over 10, regardless of their posterior shape.

Based on this, we provide two recommendations for using the debled catalog. For studies that can incorporate the full posterior probability distribution for each source, the entire catalog can be used, as the posteriors correctly capture the complex uncertainties. However, for many science cases, a simple, high-purity sample is required. For these applications, we recommend a selection based on significance. A cut of Significance > 3 provides a practical way to flag a reliable subset of detections. Given its usefulness for assessing detection reliability, we will provide the significance for each source in the final debled catalog.

4.6.4 Goodness-of-Fit: The p-value Residual Statistic

To assess the goodness-of-fit for each source, we use the Bayesian p-value residual (Gelman et al. 1996) statistic, as defined in Shirley

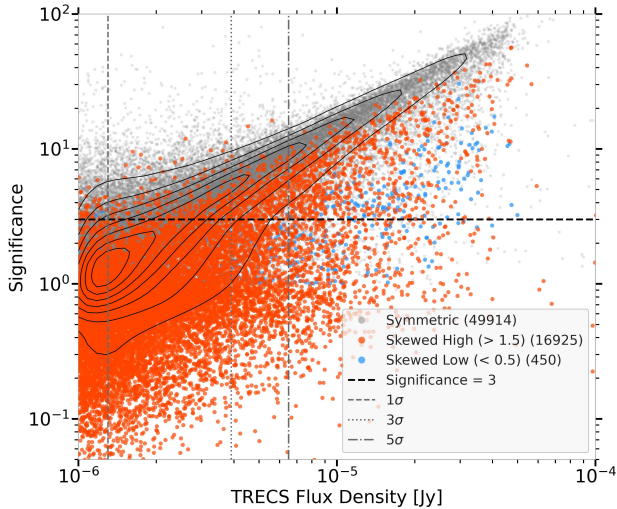


Figure 12. Recovered significance (median flux density divided by conservative uncertainty) as a function of true T-RECS input flux density for the Radio-Likely Prior, and $50 \mu\text{Jy}$ SRL mask. Points are colour-coded by posterior asymmetry: grey = symmetric posteriors, orange = skewed to high flux, blue = skewed to low flux, with black contours indicating the density of the distribution. The vertical dashed lines indicate the 1σ , 3σ , and 5σ thermal noise levels of the simulation, while the horizontal red dashed line indicates a significance of 3.

et al. (2021). This metric is a form of posterior predictive check that quantifies model fit to local data given the uncertainties. The resulting statistic is a probability, where a value of 0 indicates a model that always provides a good fit, and a value of 1 indicates a model that always provides a poor fit.

We identify sources with a p-value residual statistic > 0.6 as having an unreliable fit. This threshold is determined empirically from our simulations (see Figure 13), where it was found to effectively flag sources with significantly biased flux densities without removing a large fraction of well-fit sources. High p-values may arise when sources are poorly described by XID+’s point-source assumption, such as bright, extended sources that violate this model.

The power of the recommended strategy, Radio-Likely Prior and a $50 \mu\text{Jy}$ mask, is evident in the right panel as the fraction of sources flagged with unreliable p-values is reduced. This shows that the strategy improves both the overall flux accuracy and precision and the reliability of individual fits.

4.7 Recovery of Source Counts

A robust test of the entire process is to compare the Euclidean-normalized source counts ($S^{2.5}dN/dS$) of the recovered catalog against the true input catalog to the simulation, where the injected source population is limited to flux densities above $0.5 \mu\text{Jy}$. Figure 14 shows the source counts. First, we examine the results from our PyBDSF blind source extraction. At bright flux densities ($S_{1.4} \gtrsim 0.5 \text{ mJy}$), the SRL counts are in excellent agreement with the true T-RECS counts. At intermediate flux densities ($S_{1.4} \lesssim 0.5 \text{ mJy}$), the PyBDSF SRL catalog shows a significant upturn, a clear signature of flux boosting. Below $\sim 0.2 \text{ mJy}$, the PyBDSF counts drop off sharply as the sources in this flux range are boosted to higher flux densities.

Next, we analyze the deblended counts, which are defined only below their respective masking thresholds. The results from using

the Full Prior show a significant overestimation of the true T-RECS counts. This is because when presented with a dense, complete list of all sources, the algorithm fits low-level flux to the numerous priors, essentially promoting noise peaks into spurious low-flux detections. This effect is more pronounced for the less restrictive $250 \mu\text{Jy}$ mask, which provides a more complex environment for the algorithm.

The counts from our recommended configuration, using the Radio-Likely Prior, accurately trace the true T-RECS distribution. For the $50 \mu\text{Jy}$ mask, the deblended counts are in excellent agreement with the ground truth from $30 \mu\text{Jy}$ down to approximately $3.9 \mu\text{Jy}$ (3σ). For the $250 \mu\text{Jy}$ mask, the counts are reliable from approximately $100 \mu\text{Jy}$, to 3σ . In both cases, the counts drop off sharply below $2 \mu\text{Jy}$, due to the intrinsic incompleteness of the prior itself, which was defined with a $1 \mu\text{Jy}$ flux cut.

To quantify the statistical reliability of these results, we derive their uncertainties directly from the full posterior probability distributions. As the deblending was performed on independent tiles, the MCMC chains for each tile are statistically independent. To propagate this uncertainty, we construct a global confidence region by ranking each of the 1000 MCMC samples by their log-posterior probability within each tile. The 68 per cent confidence interval is then defined by the envelope between the source count curves derived from the highest-ranked (“best-fit”) and lowest-ranked (“worst-fit”) global samples. To avoid over-cluttering the plot, we show only these confidence intervals for the primary $50 \mu\text{Jy}$ deblending runs. As shown in Figure 14, the median-derived source counts for both the Full Prior and Radio-Likely Prior lie well within their respective 68 per cent confidence intervals. A notable feature is that the confidence intervals widen as they approach the $50 \mu\text{Jy}$ masking threshold.

Finally, results from both the large-area, varying-noise simulation (red stars) and the positional offset test (peach-yellow diamonds) show excellent agreement with the ideal case, demonstrating that our statistical determination of source counts is robust to realistic observational uncertainties.

4.8 Summary and Recommended Strategy

The simulations in Section 4.1 provide clear guidance for applying XID+ to the MIGHTEE survey. They show that deblending is essential, as standard source-finding with PyBDSF suffers from significant flux boosting in the confused regime, making it unsuitable for accurate faint-source science. The quality of the prior list is the dominant factor: a high-purity, albeit incomplete, Radio-Likely Prior, yields far more accurate flux density measurements, with a scatter of 0.3 dex at $30 \mu\text{Jy}$, than a complete but unfiltered prior, which has a scatter greater than 1 dex. These tests show that a $50 \mu\text{Jy}$ masking strategy is the best, as it improves faint-source precision and avoids a systematic underestimation bias for bright, extended sources. When combined, this optimal strategy accurately recovers the true source number counts down to the $\sim 3\sigma = 3.9 \mu\text{Jy}$.

This performance remains stable under realistic observational conditions; our stress tests with spatially varying noise and empirical positional offsets confirm that the strategy is robust to these real-world imperfections. Finally, the Bayesian p-value provides a necessary diagnostic for identifying the small fraction of poorly constrained sources. Based on these findings, our recommended strategy for the real MIGHTEE data is to use a high-confidence, Radio-Likely Prior list and apply a mask to exclude sources $> 50 \mu\text{Jy}$. We further recommend that the final catalog include the Bayesian p-value and detection significance to facilitate the selection of reliable samples.

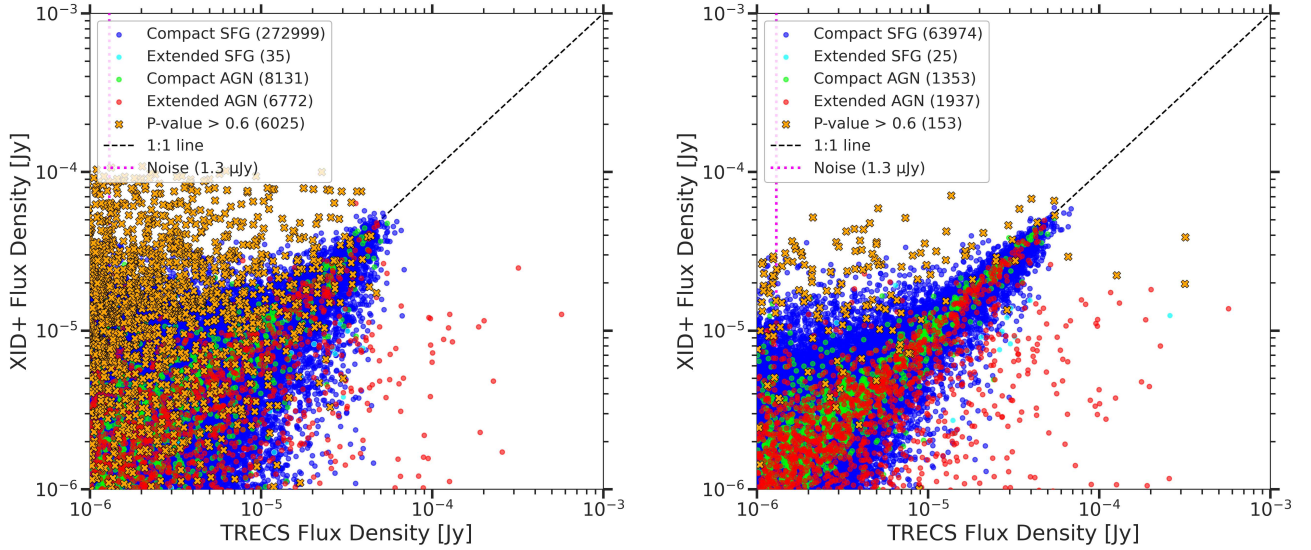


Figure 13. The effect of the Bayesian p-value as a quality flag, using the $50 \mu\text{Jy}$ SRL mask. Sources with unreliable fits ($p > 0.6$) are highlighted in orange. Left: Using the full T-RECS prior, a number of sources are flagged. Right: Using the Radio-Likely Prior, the fraction of unreliable fits is almost negligible. This shows that a high-purity prior leads to more robust fits and that the p-value statistic is an effective diagnostic for identifying outliers.

5 APPLICATION TO THE MIGHTEE-COSMOS FIELD

Having established and tested our optimal deblending strategy on realistic simulations, including spatially varying noise and positional offsets, we now apply this approach to the MIGHTEE-COSMOS low-resolution map. This section details the construction of the final prior catalog and mask, and presents the results of the deblending; the outcome is a high-fidelity source catalog and number counts.

5.1 Prior list

Based on the simulation results in Section 4, we adopt the Radio-Likely Prior as part of our deblending strategy for the primary scientific analysis. The results from this high-purity approach are presented in the main body of this section. For completeness, the results from the *Comprehensive L_{IR} Prior* are presented in Appendix C, where they serve as a valuable real-world confirmation of our simulation findings.

5.2 Masking Strategy

We applied a multi-layered masking strategy to the real data to exclude regions unsuitable for analysis. This includes masking for radio artefacts and regions of incomplete multi-wavelength data.

5.2.1 Radio Masking

Following the results from our simulations, our primary mask is generated from the PyBDSF SRL catalog by masking all sources brighter than $50 \mu\text{Jy}$. Specifically, we select all sources from the MIGHTEE DR1 SRL catalog from Hale et al. (2025) with a peak flux greater than $50 \mu\text{Jy}$ and mask them.

Beyond the primary mask validated in simulations, we adopt a more aggressive elliptical mask around the very brightest sources ($S_{1.3, \text{peak}} > 6 \text{ mJy}$). This is necessary to address observational artifacts, such as residual sidelobes from imperfect deconvolution, which

Table 3. Flux-dependent elliptical mask radii and the number of sources in each flux range (N). Radius in arcmin.

Flux Range (mJy)	Minor Radius	Major Radius	N
$6.0 \leq S_{1.3\text{GHz}} < 12.0$	0.81	1.09	48
$12.0 \leq S_{1.3\text{GHz}} < 19.0$	0.98	1.77	16
$19.0 \leq S_{1.3\text{GHz}} < 25.0$	1.50	2.47	5
$S_{1.3\text{GHz}} \geq 25.0$	1.53	2.97	20

are not present in our idealized simulations. These artifacts can extend over larger areas than the source emission itself. We determined an empirical relationship between source flux and the required elliptical mask size by measuring the extent of these artifacts around several bright sources in the MIGHTEE-COSMOS map. This relationship defines progressively larger mask radii for sources in different flux density bins (Table 3). The final radio mask is the combination of the $50 \mu\text{Jy}$ model-based mask and this additional artefact mask.

5.2.2 Stellar Masking

Finally, we mask regions around bright stars using the COSMOS2020 combined star mask (Weaver et al. 2022). We mask these regions because the multi-wavelength data used to define our prior are incomplete in these areas.

5.2.3 Final priors

Applying a combined mask, which incorporates both our radio masks and the star masks (Weaver et al. 2022), to our two raw prior lists yields the final input catalogs used for deblending. The *Comprehensive L_{IR} Prior* is reduced to 298,894 sources. The more targeted Radio-Likely Prior is reduced to 89,562 sources.

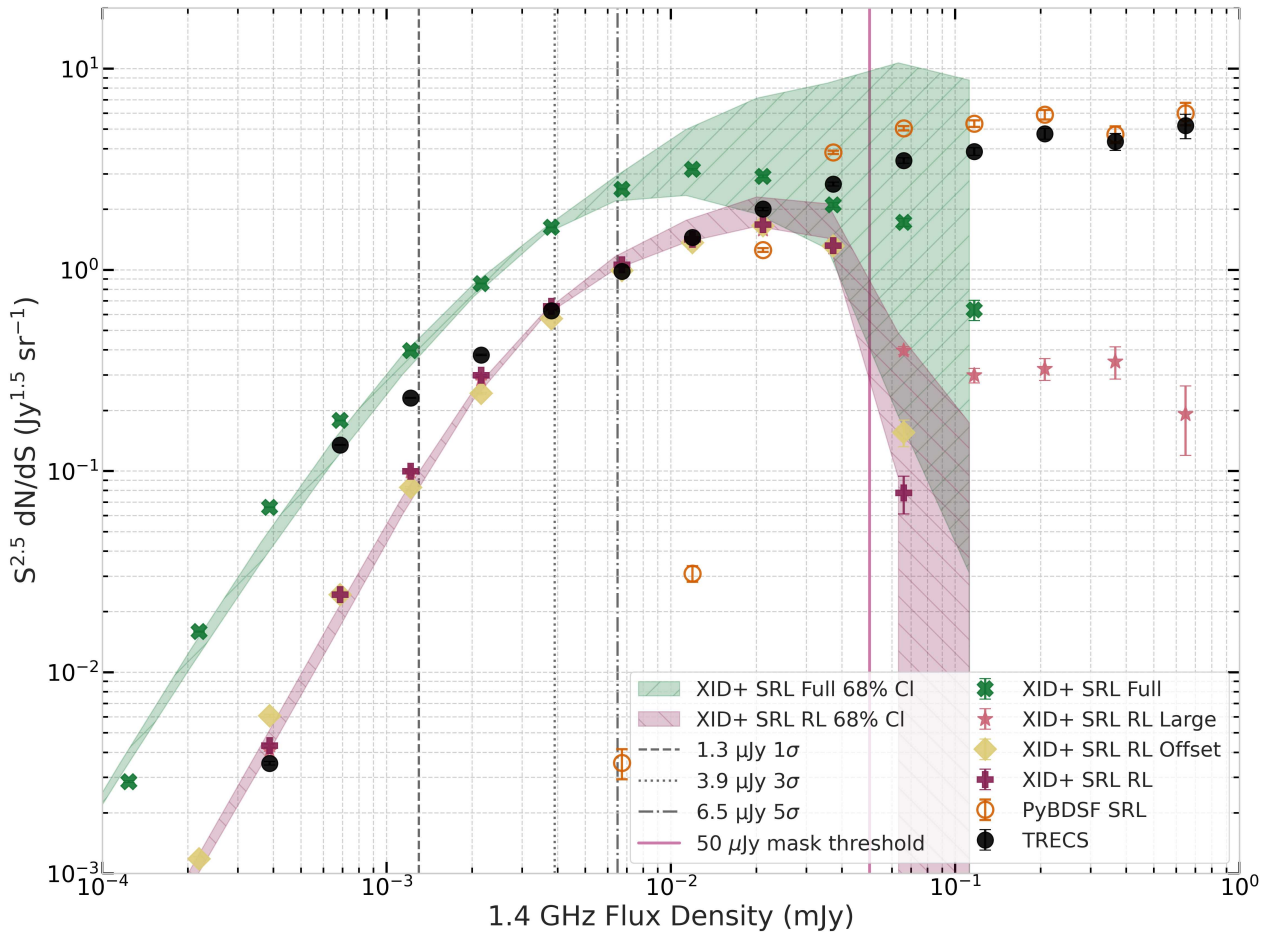


Figure 14. Euclidean-normalized 1.4 GHz source counts from the simulated data, comparing various extraction methods to the ground truth. The ground truth, injected source counts from the T-RECS simulation, are shown as solid black circles. The source counts extracted from our simulated map using the PyBDSF SRL catalog are shown as unfilled orange circles. The debiased results for the full Prior are shown as green crosses. For the Radio-Likely Prior, results are shown as dark red plus-signs. The debiased counts from our large-area, varying-noise simulation are shown as red stars. The results from the simulation incorporating positional offsets are shown as peach diamonds. All XID+ extraction runs shown here use the 50 μ Jy mask. The shaded green and pink regions represent the 68 per cent confidence intervals for the full Prior and Radio-Likely Prior debiending runs, respectively. The vertical grey lines indicate 1, 3, and 5 times the thermal noise (σ , 1.3 μ Jy). The vertical red line indicates the upper flux limit of 50 μ Jy; sources brighter than this were masked prior to debiending.

5.3 Flux Recovery and Comparison

We ran XID+ on the MIGHTEE-COSMOS map using the Radio-Likely Prior, resulting in a full debiended catalog of 89,562 sources. The primary diagnostic for the reliability of individual flux measurements is the Bayesian p-value residual statistic. Our initial debiending run, using sampler settings identical to those validated in our simulations (i.e., the Stan default `max_treedepth=10`), led to a large number of sources with poor goodness-of-fit statistics (9,238 sources, or over 10 per cent of the sample, had a Bayesian p-value > 0.6).

Further investigation showed that un-modeled artifacts and extended emission in the real MIGHTEE data produced complex posteriors that the sampler could not explore fully at the default depth, resulting in incomplete MCMC convergence. Increasing the `max_treedepth` parameter to 15 allowed the NUTS sampler to explore these posteriors more thoroughly. This computationally expensive change dramatically improved the fits, reducing the number of poorly fit sources by over 68 per cent (from 9,238 to 2,933), now representing just 3.3 per cent of the sample.

To validate our flux densities, we compare them to the independent analysis of the MIGHTEE data using the super-debended technique (Jin et al. 2018; Liu et al. 2018). This approach performs PSF-fitting at prior positions derived from deep ancillary data. We use the updated catalog (Jin et al. 2018, 2022, 2024), which was constructed using priors from the COSMOS2020 (Weaver et al. 2022), VLA 3GHz (Smolčić et al. 2017), and A3COSMOS (Liu et al. 2019) catalogs. This dataset serves as a robust benchmark because the super-debended flux densities and errors were rigorously calibrated to quasi-Gaussian uncertainties using Monte Carlo simulations performed directly on the real map (Jin et al. 2018; Liu et al. 2018). This specific dataset has been used to derive radio properties in several recent studies (e.g., An et al. 2021; Delvecchio et al. 2021; Sillassen et al. 2024)

We cross-matched our full Radio-Likely Prior catalog (89,562 sources) with the super-debended catalog using a 0.3 arcsec radius, finding 88,939 matches. As shown in Figure 15, the two methods show excellent agreement for the bulk of the population, as they lie tightly along the 1:1 line with some scatter. The sources flagged with a high p-value in our analysis (dark green points) are mostly those

that form the outlier population where our XID+ flux densities are systematically higher than the super-deblended values. This confirms that the p-value is an effective diagnostic for identifying potentially unreliable flux measurements.

Our final data product is a complete catalog of 89,562 sources. For each source, we provide the Bayesian p-value statistic, which assesses the goodness of fit, and the detection significance. We do not remove sources from the catalog, as the full posterior distributions for low-significance sources remain statistically valid for stacking or ensemble analyses.

However, for applications requiring robust individual source detections, we first consider a simple significance-based selection. Applying the criterion defined in Section 4.6.3 (Significance > 3) yields 31,779 sources, while a flux density cut above the average 3σ limit ($4.8 \mu\text{Jy}$) yields 31,083 sources. To construct a highly conservative recommended sample, we select sources that satisfy both of these criteria simultaneously and exhibit a reliable goodness-of-fit (p-value residual statistic < 0.6). This rigorous selection results in a high-fidelity catalog of 20,757 sources.

5.4 Uncertainty Characterization

As predicted by our simulations (Section 4.6), the flux density uncertainties for the real data exhibit a skewed nature for faint sources near the noise limit, reflecting the physical non-negativity constraint on flux density. Figure 16 demonstrates this behavior, showing that the ratio of the upper-to-lower uncertainty is close to 1 for bright sources but increases systematically as flux densities approach the thermal noise (σ) of the map. This confirms that our analysis captures the expected complex posterior distributions for the faint source population.

5.5 Radio Source Number Counts

The primary scientific product of this work is the 1.4 GHz radio source number counts. The flux densities have been converted from the native MIGHTEE observing frequency to 1.4 GHz using the spatially varying frequency-response maps of Hale et al. (2025), adopting a spectral index $\alpha = 0.7$. In Figure 17, we present the Euclidean-normalized source counts derived from our *Comprehensive* and *Radio-Likely Prior* catalogs. Our primary result, from the *Radio-Likely Prior*, shows excellent agreement with the literature at certain flux ranges. At the bright end of our deblended range, from approximately 20 to $40 \mu\text{Jy}$, our counts lie below the completeness-corrected literature values from Hale et al. (2025). This turnover is expected from the $50 \mu\text{Jy}$ mask and a similar behavior is seen in the simulations (see Figure 14), confirming that this is a feature of our methodology, not a discrepancy in the measurement.

Moving deeper into the confusion-dominated regime in MIGHTEE, from approximately $15 \mu\text{Jy}$ down to our faintest reliable bin at $\sim 4.8 \mu\text{Jy}$ (3σ), our counts show excellent agreement with the P(D) analysis of the MeerKAT DEEP2 field from Matthews et al. (2021a). The agreement between our catalog-based deblended counts and this independent statistical measurement validates our methodology in a flux density regime where traditional source-finding fails due to confusion. This implies that we are resolving the vast majority of the radio background at these flux densities.

Below this 3σ limit, our counts decline and fall below the P(D) result. This decline is expected since, based on the analysis of the simulations, below 3σ the flux densities of the *Radio-Likely Prior* source counts systematically and increasingly underestimate

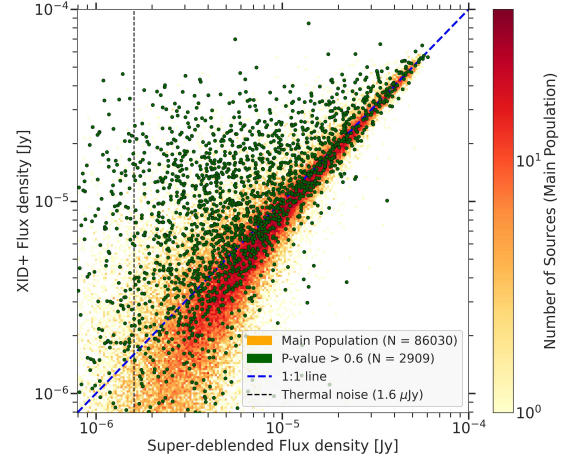


Figure 15. Comparison between XID+ *Radio-Likely Prior* flux densities from this work and the super-deblended flux densities (An et al. 2021; Jin et al. 2024) for 88,939 matched sources. Sources with an unreliable fit (Bayesian p-value > 0.6) are highlighted as dark green markers.

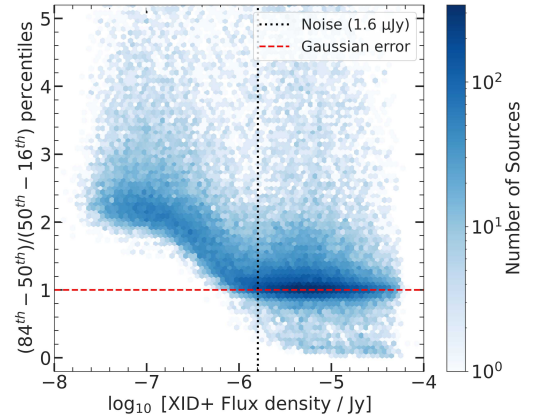


Figure 16. The ratio of the upper to lower flux density uncertainty as a function of the deblended XID+ flux for sources from the *Radio-Likely Prior*. The ratio increases for faint sources, correctly capturing the skewed posterior distribution near the noise limit.

the ground truth. Although we note that the only observational constraints on the true form of the source counts at these flux densities come from the P(D) analysis of Matthews et al. (2021a), where optical counterparts are not required.

In contrast, the counts derived from the sub-optimal *Comprehensive L_{IR} Prior* (shown in Figure 17, see Appendix C) are systematically higher below 5σ . This result from real data confirms the prediction from our simulations: an inclusive but low-purity prior leads to an over-deblending effect that artificially boosts the number of faint sources. Intriguingly, at the faintest flux limits ($\sim 1-2\sigma$), these overestimated counts from the *Comprehensive Prior* appear to align with the P(D) results. This provides real-data confirmation of our primary simulation finding: an unfiltered prior will indeed generate a large population of spurious sources, but in doing so, it can statistically approximate the true underlying source population. This highlights both the remarkable accuracy of P(D) analysis in the confusion-dominated regime and the complementary power of our deblending method, which provides reliable flux densities for a pure, albeit incomplete, sample of individual sources.

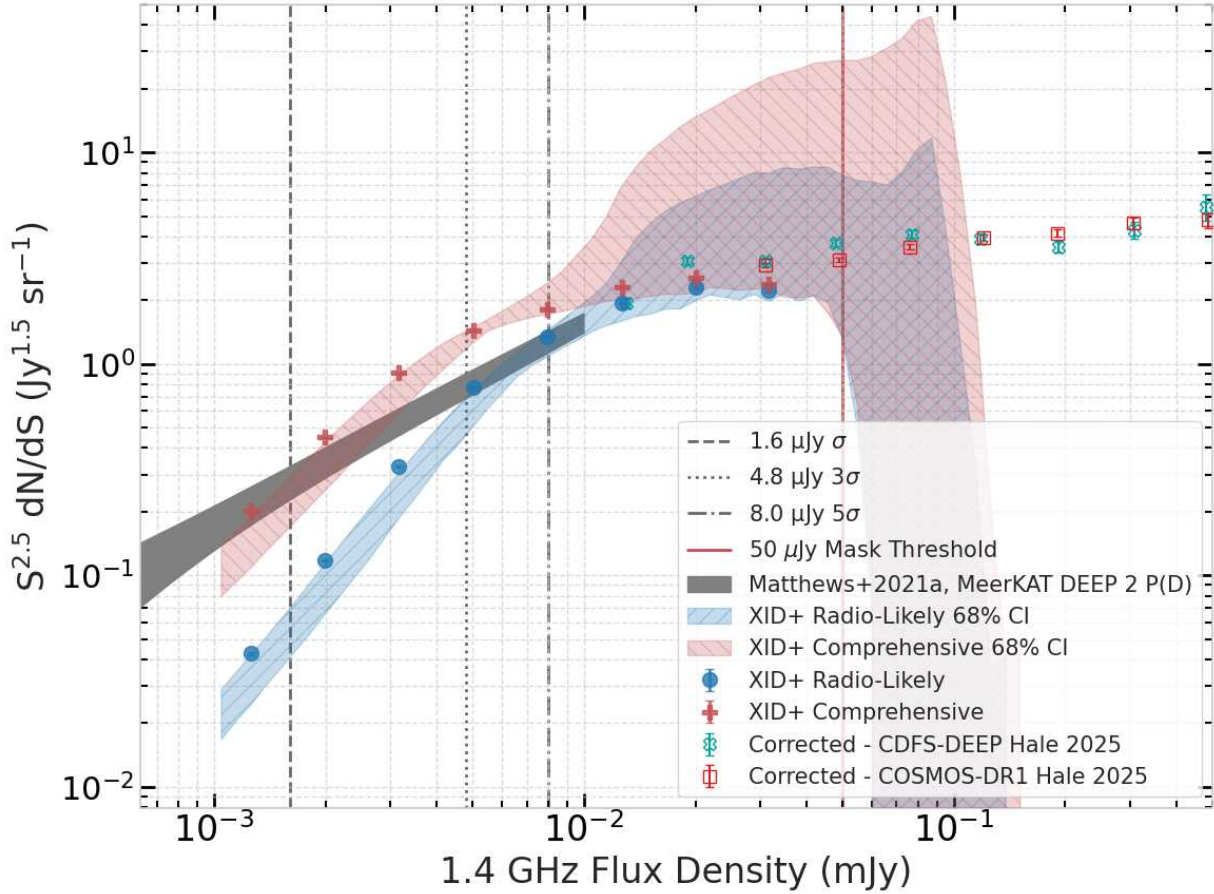


Figure 17. Euclidean-normalized 1.4 GHz radio source counts. The deblended counts from our optimal Radio-Likely Prior are shown as blue filled circles, while the results from the *Comprehensive* L_{IR} Prior are shown as red crosses. The blue and red shaded regions represent the 68% confidence intervals for these measurements, respectively. For comparison, we plot several data points from recent literature. From the MIGHTTEE DR1 (Hale et al. 2025), the completeness-corrected counts for the COSMOS (red unfilled squares) and the CDFS-DEEP (cyan x-markers). The grey shaded region represents the P(D) analysis of the MeerKAT DEEP2 field from Matthews et al. (2021a). Vertical dashed, dotted, and dash-dotted grey lines indicate 1, 3, and 5 times the central thermal noise of the map ($\sigma = 1.6 \mu\text{Jy}$), respectively. The solid vertical red line indicates the upper flux limit of $50 \mu\text{Jy}$; sources brighter than this were masked prior to deblending.

6 CONCLUSIONS AND FUTURE WORK

Deep radio continuum surveys from highly sensitive facilities like MeerKAT provide unprecedented access to the faint radio source population, enabling important tests of galaxy evolution models. However, their scientific potential is fundamentally limited by source confusion in the absence of appropriate analysis techniques. We have developed, validated, and applied a complete framework for producing high-fidelity deblended radio source catalogs from confusion-limited survey data, using the MIGHTTEE-COSMOS field as our primary application. Our key findings and contributions are:

(i) Deblending is essential for deep confused radio surveys: We confirm through simulations that standard source-finding suffers from significant flux boosting in the confused regime, making it unsuitable for accurate faint-source science.

(ii) XID+ is an effective tool for radio deblending: We have adapted and validated the probabilistic Bayesian framework XID+ for the specific challenges of deep radio continuum data. When configured with an appropriate prior list and masking strategy, it accurately

recovers both individual source flux densities and the statistical distribution of the underlying source population.

(iii) Prior quality governs deblending accuracy: The reliability of deblended flux densities is sensitive to the purity of the prior list. Our simulations and real-data application both show that a high-purity, albeit incomplete, prior (our Radio-Likely Prior) yields far more precise and accurate flux measurements (with a scatter of ≈ 0.3 dex at $30 \mu\text{Jy}$ in simulations). In contrast, a complete but unfiltered prior leads to over-deblending, resulting in large, unreliable flux density uncertainties (>1 dex scatter) and a proliferation of spurious faint detections.

(iv) This work delivers the deepest catalog-based MIGHTTEE-COSMOS source counts to date. When applied to the MIGHTTEE-COSMOS field, our validated strategy recovers the 1.4 GHz source number counts down to the 3σ limit ($4.8 \mu\text{Jy}$). The final catalog contains 89,562 sources, including a recommended high-fidelity subset of 20,757 sources.

(v) Bayesian diagnostics and sampler optimization are important for ensuring catalog fidelity: The Bayesian p-value residual statistic is a powerful tool for identifying sources with potentially unreliable flux

measurements. We find that its successful application to complex, real-world data requires careful tuning of the MCMC sampler settings within the Stan framework. Increasing the `max_treedepth` from the default of 10 to 15 was required for convergence on robust solutions, though with increased computational cost. This demonstrates that the increased complexity of real data requires a more exhaustive exploration of the posterior parameter space to achieve reliable fits.

This deblending framework enables a wide range of science applications beyond what is possible with traditional source-finding. These include constructing a complete, dust-unbiased census of the cosmic star formation history (e.g. Novak et al. 2017; Matthews et al. 2024); probing the evolution of the infrared–radio correlation to unprecedented depths (e.g. Delhaize et al. 2017; Delvecchio et al. 2021; Moloko et al. 2025); disentangling star formation and AGN activity in radio-quiet AGN (e.g. Padovani 2016; Panessa et al. 2019) and precisely measuring the faint-end slope of the radio luminosity function (e.g. Smolčić et al. 2017; Algera et al. 2020). The framework established in this work is directly applicable to other confusion-limited radio surveys from current facilities (ASKAP, LOFAR, VLA, uGMRT).

While the framework established in this work provides a validated approach for producing deep, reliable deblended radio source catalogs, it could be refined further.

Specifically, in the current framework, we assume that the sources that lie at these faint flux densities are both unresolved (a reasonable assumption) and that their flux density is distributed over the restoring beam. However, the maps that we use are not cleaned to the levels that we are extracting the flux densities from, as such, we should use the synthesised beam as our PSF rather than the restoring beam, whose information is in the headers. However, this would introduce additional complexity without a significant amount of gain. The synthesised beam for the MIGHTEE data is tapered to produce a Gaussian-like profile that is very similar to the adopted restoring beam. As such, the difference between using the restoring beam approximation and the full synthesised beam is of the order 5 per cent, significantly less than the uncertainties on individual sources. However, ideally, one would simulate the full observational pipeline: Using the improved sky model, one could simulate the entire data acquisition and reduction process. This involves generating the raw instrumental visibilities, introducing realistic thermal noise and calibration errors, and then processing these data through the identical imaging and deconvolution pipeline used for the MIGHTEE observations. This approach would naturally produce complex artifacts, such as residual sidelobes and spatially correlated noise, providing the ultimate test of this methodology against real-world instrumental effects. However, this would be very computationally intensive.

One could also improve the Radio-Likely Prior with more advanced source selection. The success of our deblending is highly dependent on the purity of the Radio-Likely Prior. While effective, the current method based on the IRRC can be advanced by using more sophisticated predictive models. Future work will explore the use of full-SED models to measure the SFR and/or machine learning algorithms trained on the rich, multi-wavelength photometry available in the COSMOS field, similar to (Wang et al. 2024a) to learn the complex relationship between a galaxy’s full UV-to-mid-infrared spectral energy distribution and its expected 1.4 GHz flux. This would allow us to generate a more nuanced, probabilistic radio flux estimate for every source in the parent catalog, creating a more robust and complete Radio-Likely Prior that better distinguishes detectable radio sources from undetectable ones.

ACKNOWLEDGEMENTS

EM acknowledges financial support from the University of South Africa (Research Fund: 409000). MJJ, CLH and IHW acknowledges support from the Hintze Family Charitable Foundation through the Oxford Hintze Centre for Astrophysical Surveys. MJJ acknowledges the support of the STFC consolidated grant [ST/S000488/1] and [ST/W000903/1] and from a UKRI Frontiers Research Grant [EP/X026639/1]. MGS acknowledges support from the South African National Research Foundation (Grant No. 84156). DJBS acknowledges support from the UK’s Science and Technology Facilities Council via grant ST/Y001028/1, and from the Leverhulme Trust via Research Project Grant RPG-2025-078. CLH acknowledges support from STFC through grant ST/Y000951/1. MV acknowledges financial support from the Inter-University Institute for Data Intensive Astronomy (IDIA), a partnership of the University of Cape Town, the University of Pretoria and the University of the Western Cape, and from the South African Department of Science and Innovation’s National Research Foundation under the ISARP RADIOMAP Joint Research Scheme (DSI-NRF Grant Number 150551) and the CPRR HIPPO Project (DSI-NRF Grant Number SRUG22031677). SJ acknowledges the European Union’s Horizon Europe research and innovation program under the Marie Skłodowska-Curie Action grant No. 101060888, and the Villum Fonden research grants 37440 and 13160. FXA acknowledges the support from the National Natural Science Foundation of China (12303016) and the Natural Science Foundation of Jiangsu Province (BK20242115). The authors thank Suman Chatterjee, Antonio la Marca, and Lingyu Wang for helpful discussions that enhanced this work.

The MeerKAT telescope is operated by the South African Radio Astronomy Observatory, which is a facility of the National Research Foundation, an agency of the Department of Science and Innovation. We acknowledge the use of the ilifu cloud computing facility – www.ilifu.ac.za, a partnership between the University of Cape Town, the University of the Western Cape, Stellenbosch University, Sol Plaatje University and the Cape Peninsula University of Technology. The ilifu facility is supported by contributions from the Inter-University Institute for Data Intensive Astronomy (IDIA – a partnership between the University of Cape Town, the University of Pretoria and the University of the Western Cape), the Computational Biology division at UCT and the Data Intensive Research Initiative of South Africa (DIRISA). The authors acknowledge the Centre for High Performance Computing (CHPC), South Africa, for providing computational resources to this research project. This work made use of the CARTA (Cube Analysis and Rendering Tool for Astronomy) software (DOI 10.5281/zenodo.3377984 – <https://cartavis.github.io>). EM acknowledges the use of AI-based tools for assistance with code development and for improving the clarity and language of the manuscript.

DATA AVAILABILITY

The MIGHTEE DR1 data products are available at <https://doi.org/10.48479/7msw-r692>. The final deblended catalog presented in this paper will be made available upon publication.

REFERENCES

Adams N. J., Bowler R. A. A., Jarvis M. J., Häußler B., Lagos C. D. P., 2021, *MNRAS*, 506, 4933

- Aihara H., AlSaiyad Y., Ando M., Armstrong R., Bosch J., Egami E., et al. 2019, *PASJ*, 71, 114
- Aihara H., et al., 2022, *PASJ*, 74, 247
- Algera H. S. B., et al., 2020, *ApJ*, 903, 139
- An F., et al., 2021, *MNRAS*, 507, 2643
- Becht E., McInnes L., Healy J., Dutertre C., Kwok I. W. H., Ng L. G., Ginhoux F., Newell E. W., 2019, *Nature Biotechnology*, 37, 38
- Bell E. F., 2003, *ApJ*, 586, 794
- Best P. N., Heckman T. M., 2012, *MNRAS*, 421, 1569
- B  thermin M., Dole H., Cousin M., Bavouzet N., 2010, *A&A*, 516, A43
- Blandford R. D., Konigl A., 1979, *ApJ*, 232, 34
- Blandford R. D., Rees M. J., 1974, *MNRAS*, 169, 395
- Bonaldi A., Bonato M., Galluzzi V., Harrison I., Massardi M., Kay S., De Zotti G., Brown M. L., 2019, *MNRAS*, 482, 2
- Bonaldi A., Hartley P., Ronconi T., De Zotti G., Bonato M., 2023, *MNRAS*, 524, 993
- Bonfield D. G., et al., 2011, *MNRAS*, 416, 13
- Bonzini M., et al., 2013, *MNRAS*, 436, 3759
- Booth R. S., de Blok W. J. G., Jonas J. L., Fanaroff B., 2009, *arXiv e-prints*, p. [arXiv:0910.2935](https://arxiv.org/abs/0910.2935)
- Brammer G. B., van Dokkum P. G., Coppi P., 2008, *ApJ*, 686, 1503
- Braun R., Bourke T., Green J. A., Keane E., Wagg J., 2015, in *Advancing Astrophysics with the Square Kilometre Array (ASKAP)*. p. 174, doi:10.22323/1.215.0174
- Carpenter B., et al., 2017, *Journal of Statistical Software*, 76, 1
- Chapin E. L., et al., 2011, *MNRAS*, 411, 505
- Condon J. J., 1974, *ApJ*, 188, 279
- Condon J. J., 1984, *ApJ*, 287, 461
- Condon J. J., 1992, *ARA&A*, 30, 575
- Condon J. J., et al., 2012, *The Astrophysical Journal*, 758
- Condon J. J., Kellermann K. I., Kimball A. E., Ivezi c  ., Perley R. A., 2013, *ApJ*, 768, 37
- Conroy C., Gunn J. E., White M., 2009, *ApJ*, 699, 486
- Cook R. H. W., et al., 2024a, *Monthly Notices of the Royal Astronomical Society*, 531, 708
- Cook T. L., et al., 2024b, *MNRAS*, 535, 2129
- Delhaize J., et al., 2017, *A&A*, 602, A4
- Delvecchio I., et al., 2021, *A&A*, 647, A123
- Driessen L. N., et al., 2024, *Publ. Astron. Soc. Australia*, 41, e084
- Egbo O. D., Buckley D. A. H., Groot P. J., Cavallaro F., Woudt P. A., Thompson M. A., Mutale M., Bietenholz M., 2025, *MNRAS*, 540, 2685
- Euclid Collaboration Moneti A., McCracken H. J., Shuntov M., Kauffmann O. B., Capak P., et al. 2022, *A&A*, 658, A126
- Fanaroff B. L., Riley J. M., 1974, *MNRAS*, 167, 31P
- Fazio G. G., et al., 2004, *ApJS*, 154, 10
- Fotopoulou S., 2024, *Astronomy and Computing*, 48, 100851
- Gelman A., Meng X.-L., Stern H., 1996, *Statistica Sinica*, 6, 733
- Giri G., Fendt C., Thorat K., Bodo G., Rossi P., 2024, *Frontiers in Astronomy and Space Sciences*, 11, 1371101
- G rski K. M., Hivon E., Banday A. J., Wandelt B. D., Hansen F. K., Reinecke M., Bartelmann M., 2005, *ApJ*, 622, 759
- Gupta Y., et al., 2017, *Current Science*, 113, 707
- G rkan G., et al., 2015, *MNRAS*, 452, 3776
- G rkan G., et al., 2018, *MNRAS*, 475, 3010
- Gwyn S. D. J., 2012, *AJ*, 143, 38
- Hale C. L., et al., 2022, *Monthly Notices of the Royal Astronomical Society*, 520, 2668
- Hale C. L., et al., 2025, *MNRAS*, 536, 2187
- Hardcastle M. J., Croston J. H., 2020, *New Astron. Rev.*, 88, 101539
- Harrison I., et al., 2020, *MNRAS*, 495, 1737
- Helou G., Soifer B. T., Rowan-Robinson M., 1985, *ApJ*, 298, L7
- Hewett P. C., Warren S. J., Leggett S. K., Hodgkin S. T., 2006, *MNRAS*, 367, 454
- Heywood I., et al., 2021, *Monthly Notices of the Royal Astronomical Society*, 509, 2150–2168
- Hickox R. C., Mullaney J. R., Alexander D. M., Chen C.-T. J., Civano F. M., Goulding A. D., Hainline K. N., 2014, *ApJ*, 782, 9
- Hoffman M. D., Gelman A., 2014, *Journal of Machine Learning Research*, 15, 1593
- Hurley P. D., et al., 2017, *MNRAS*, 464, 885
- Hwang H.-C., Zakamska N. L., Alexandroff R. M., Hamann F., Greene J. E., Perrotta S., Richards G. T., 2018, *Monthly Notices of the Royal Astronomical Society*, 477, 830
- Jarvis M. J., Rawlings S., 2004, *New Astron. Rev.*, 48, 1173
- Jarvis M. J., et al., 2010, *MNRAS*, 409, 92
- Jarvis M. J., et al., 2013, *MNRAS*, 428, 1281
- Jarvis M., et al., 2015, in *Advancing Astrophysics with the Square Kilometre Array (ASKAP)*. p. 68 ([arXiv:1412.5753](https://arxiv.org/abs/1412.5753)), doi:10.22323/1.215.0068
- Jarvis M., et al., 2016, The MeerKAT International GHz Tiered Extragalactic Exploration (MIGHTEE) Survey ([arXiv:1709.01901](https://arxiv.org/abs/1709.01901)), doi:10.22323/1.277.0006
- Jauncey D. L., 1968, *ApJ*, 152, 647
- Jin S., et al., 2018, *ApJ*, 864, 56
- Jin S., et al., 2022, *A&A*, 665, A3
- Jin S., et al., 2024, *A&A*, 690, L16
- Johnston S., et al., 2008, *Experimental Astronomy*, 22, 151
- Jolliffe I. T., Cadima J., 2016, *Philosophical transactions. Series A, Mathematical, physical, and engineering sciences*, 374, 20150202
- Jonas J. L., 2009, *Proceedings of the IEEE*, 97, 1522
- Karim A., et al., 2011, *ApJ*, 730, 61
- Kellermann K. I., Sramek R., Schmidt M., Shaffer D. B., Green R., 1989, *AJ*, 98, 1195
- Kennicutt R. C., Evans N. J., 2012, *ARA&A*, 50, 531
- Kimball A. E., et al., 2011, *ApJ*, 739, L29
- Kondapally R., et al., 2025, *MNRAS*, 536, 554
- Laigle C., McCracken H. J., Ilbert O., Hsieh B. C., Davidzon I., Capak P., et al. 2016, *ApJS*, 224, 24
- Laing R. A., Bridle A. H., 2002, *MNRAS*, 336, 328
- Lee N., et al., 2013, *ApJ*, 778, 131
- Liu D., et al., 2018, *ApJ*, 853, 172
- Liu D., et al., 2019, *ApJ*, 887, 235
- Logan C. H. A., Fotopoulou S., 2020, *A&A*, 633, A154
- Macfarlane C., et al., 2021, *MNRAS*, 506, 5888
- Magdis G. E., et al., 2012, *ApJ*, 760, 6
- Magnelli B., et al., 2010, *A&A*, 518, L28
- Magnelli B., et al., 2015, *A&A*, 573, A45
- Malefahlo E., Santos M. G., Jarvis M. J., White S. V., Zwart J. T. L., 2020, *MNRAS*, 492, 5297
- Malefahlo E. D., Jarvis M. J., Santos M. G., White S. V., Adams N. J., Bowler R. A. A., 2022, *MNRAS*, 509, 4291
- Matthews A. M., Condon J. J., Cotton W. D., Mauch T., 2021a, *The Astrophysical Journal*, 909, 193
- Matthews A. M., Condon J. J., Cotton W. D., Mauch T., 2021b, *ApJ*, 914, 126
- Matthews A. M., et al., 2024, *ApJ*, 966, 194
- Mauduit J. C., et al., 2012, *PASP*, 124, 714
- McCracken H. J., et al., 2012, *A&A*, 544, A156
- McInnes L., Healy J., Astels S., 2017, *Journal of Open Source Software*, 2, 205
- McInnes L., Healy J., Melville J., 2018, *arXiv e-prints*, p. [arXiv:1802.03426](https://arxiv.org/abs/1802.03426)
- Mingo B., et al., 2019, *MNRAS*, 488, 2701
- Mohan N., Rafferty D., 2015, PyBDSF: Python Blob Detection and Source Finder. *Astrophysics Source Code Library*, record ascl:1502.007
- Moloko M. E., Marchetti L., Jarrett T. H., Condon J. J., Cotton W. D., Matthews A. M., Mauch T., Vaccari M., 2025, *MNRAS*, 543, 2463
- Murphy E. J., et al., 2011, *ApJ*, 737, 67
- Murphy E. J., et al., 2018, *Astronomical Society of the Pacific Conference Series*, 517, 3
- Novak M., et al., 2017, *A&A*, 602, A5
- Ocran E. F., Taylor A. R., Vaccari M., Ishwara-Chandra C. H., Prandoni I., Prescott M., Mancuso C., 2020, *MNRAS*, 491, 5911
- Padovani P., 2016, *A&ARv*, 24, 13
- Panessa F., Baldi R. D., Laor A., Padovani P., Behar E., McHardy I., 2019, *Nature Astronomy*, 3, 387

- Pearson W. J., Wang L., van der Tak F. F. S., Hurley P. D., Burgarella D., Oliver S. J., 2017, *A&A*, 603, A102
- Pedregosa F., et al., 2011, *Journal of Machine Learning Research*, 12, 2825
- Rankine A. L., Matthews J. H., Hewett P. C., Banerji M., Morabito L. K., Richards G. T., 2021, *MNRAS*, 502, 4154
- Read S. C., et al., 2018, *MNRAS*, 480, 5625
- Roseboom I. G., et al., 2010, *MNRAS*, 409, 48
- Rowe B. T. P., et al., 2015, *Astronomy and Computing*, 10, 121
- Sawicki M., Arnouts S., Coupon J., Golob A., Gwyn S., Hudelot P., et al. 2019, *MNRAS*, 489, 5202
- Scheuer P. A. G., 1957, *Proceedings of the Cambridge Philosophical Society*, 53, 764
- Scoville N., et al., 2007, *ApJS*, 172, 1
- Sérsic J. L., 1963, *Boletín de la Asociación Argentina de Astronomía La Plata Argentina*, 6, 41
- Shimwell T. W., et al., 2025, *A&A*, 695, A80
- Shirley R., et al., 2021, *MNRAS*, 507, 129
- Sillassen N. B., et al., 2024, *A&A*, 690, A55
- Smith D. J. B., et al., 2021, *A&A*, 648, A6
- Smolčić V., et al., 2017, *A&A*, 602, A1
- Strateva I., et al., 2001, *AJ*, 122, 1861
- Tibshirani R., 1996, *Journal of the Royal Statistical Society Series B (Methodological)*, 58, 267
- Varadaraj R. G., Bowler R. A. A., Jarvis M. J., Adams N. J., Häußler B., 2023, *MNRAS*, 524, 4586
- Vernstrom T., et al., 2014, *MNRAS*, 440, 2791
- Wang L., et al., 2014, *MNRAS*, 444, 2870
- Wang W., Yuan Z., Yu H., Mao J., 2024a, *A&A*, 683, A174
- Wang L., et al., 2024b, *A&A*, 688, A20
- Wang Y., et al., 2025, arXiv e-prints, p. arXiv:2506.03970
- Weaver J. R., et al., 2022, *ApJS*, 258, 11
- White S. V., Jarvis M. J., Häußler B., Maddox N., 2015, *MNRAS*, 448, 2665
- White S. V., Jarvis M. J., Kalfountzou E., Hardcastle M. J., Verma A., Cao Orjales J. M., Stevens J., 2017, *MNRAS*, 468, 217
- Whittam I. H., et al., 2022, *MNRAS*, 516, 245
- Whittam I. H., et al., 2024, *MNRAS*, 527, 3231
- Whittam I. H., et al., 2025, *MNRAS*, 543, 507
- Wilman R. J., et al., 2008, *MNRAS*, 388, 1335
- Windhorst R. A., Miley G. K., Owen F. N., Kron R. G., Koo D. C., 1985, *ApJ*, 289, 494
- Yue B. H., et al., 2024, *MNRAS*, 529, 3939
- Yun M. S., Reddy N. A., Condon J. J., 2001, *ApJ*, 554, 803
- Zou H., 2006, *Journal of the American Statistical Association*, 101, 1418
- Zwart J., et al., 2015, in *Advancing Astrophysics with the Square Kilometre Array (AASKA14)*. p. 172 (arXiv:1412.5743), doi:10.22323/1.215.0172
- de Zotti G., Massardi M., Negrello M., Wall J., 2010, *A&ARv*, 18, 1
- van Haarlem M. P., et al., 2013, *A&A*, 556, A2

APPENDIX A: CORNER PLOTS FOR STAR-GALAXY CLASSIFICATION

To supplement the two-dimensional UMAP projections shown in the main text, Figure A1 shows the corner plot for all the 10-dimensional reduced feature space for the HSC+VISTA dataset. This plot illustrates how the separation between the stellar and galactic clusters is maintained across the various pairings of the reduced UMAP dimensions, reinforcing the robustness of the classification.

APPENDIX B: DEBLENDING PERFORMANCE WITH GAUL-BASED MASKING

To supplement the primary analysis presented in Section 4.4.4, we also investigated the impact of using a bright-source mask generated

from the PyBDSF GAUL catalog instead of the SRL (source list) catalog. The GAUL catalog treats every detected Gaussian component individually, making it a useful alternative to test the robustness of our masking strategy.

The deblending performance plots for this test are presented in Figures B1 and B2. The results are qualitatively and quantitatively very similar to those derived using the SRL mask in the main text. This confirms that our main conclusion, that the quality of the prior list and the $> 50 \mu$ Jy masking threshold are the dominant factors driving the fidelity of the deblended flux densities is robust and not sensitive to the specific catalog type used to generate the bright-source mask.

APPENDIX C: DEBLENDING WITH A COMPREHENSIVE L_{IR} PRIOR

To provide a real-world validation of our simulation results (Sec. 4), we also performed a deblending run on the MIGHTEE data using *Comprehensive L_{IR} Prior*. This prior was designed to be as inclusive as possible, containing 298,894 potential sources after masking, and is analogous to the "Full Prior" used in our simulations. Using the same optimized sampler settings as for the Radio-Likely Prior (`max_treedepth` up to 15), we find that 6,675 sources have a poor fit (p -value > 0.6), a dramatic reduction from the 22,133 flagged in the initial run. However, even with optimized settings, a prominent cloud of sources with significantly overestimated flux densities remains when compared to the independent super-deblended catalog. While the fraction of flagged sources has dropped to ~ 2.2 per cent of the total sample, the overall scatter in the flux comparison is visibly larger than in the Radio-Likely Prior case.

The most important outcome is seen in the source counts (Figure 17). The source counts (Figure 17) derived from this comprehensive prior are systematically higher than both our final Radio-Likely counts and the literature values. Likely due to over-deblending, where the algorithm incorrectly assigns flux to numerous faint, undetectable priors, artificially boosting the number of faint sources.

This exercise demonstrates that the choice of prior is not merely a minor technical detail but a critical factor that directly impacts the final scientific conclusions. It validates our decision to focus the main body of this paper on the results from the carefully constructed, high-purity Radio-Likely Prior.

APPENDIX D: SUPPLEMENTARY DATA TABLES

The data tables for the derived source counts and a description of the final deblended source catalog.

D1 Radio Source Counts Data

The Euclidean-normalized source counts derived from the final, quality-filtered Radio-Likely Prior catalog are provided in Table D1. These data points are plotted in Figure 17.

D2 Deblended Catalog Format

The format and column descriptions for the final deblended MIGHTEE radio point source catalog are provided in Table D2.

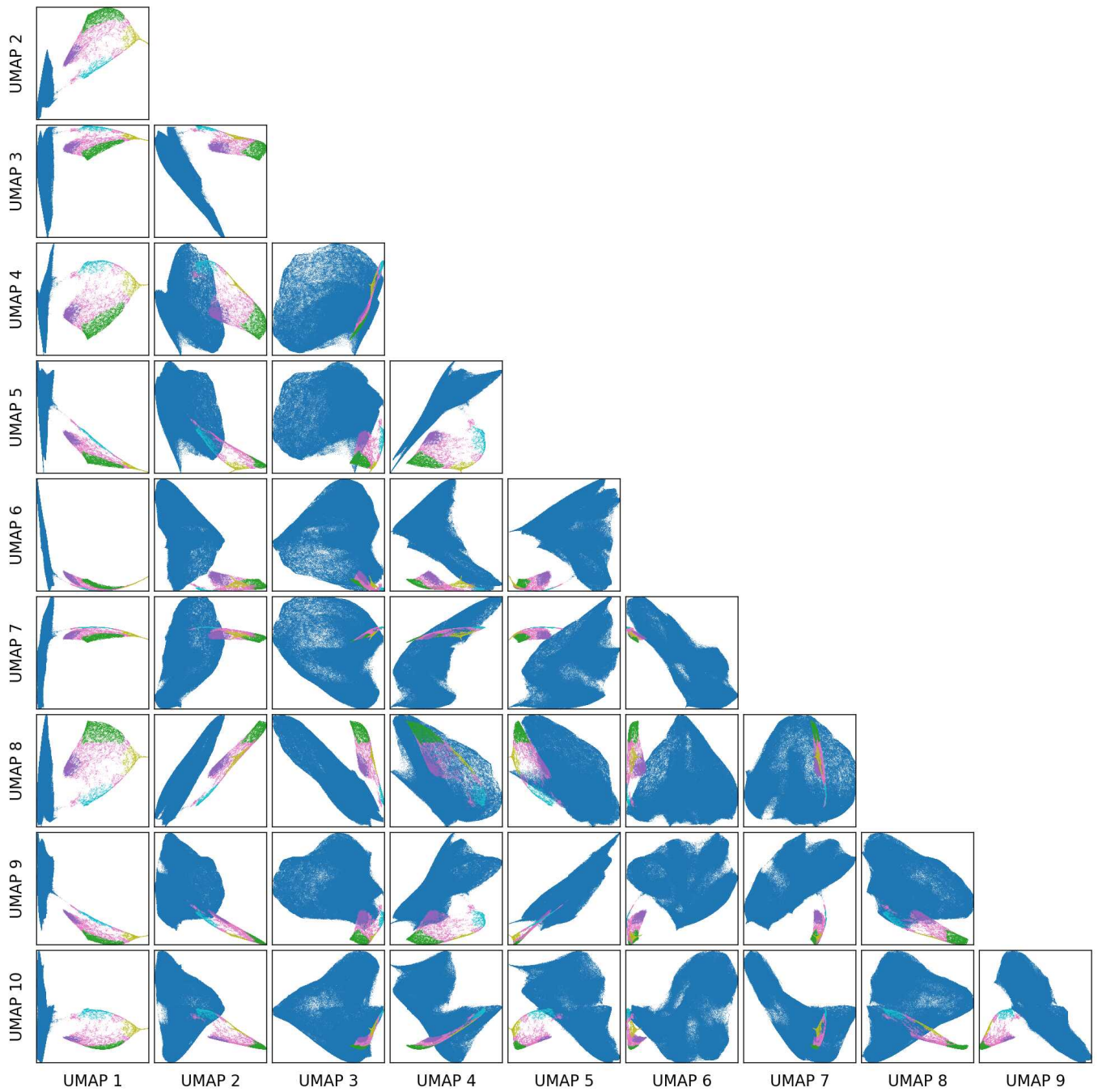


Figure A1. Corner plot of the 10 UMAP dimensions for the HSC+UltraVista dataset. Colors are consistent with Figure 1, showing how clusters separate across different dimensional pairings.

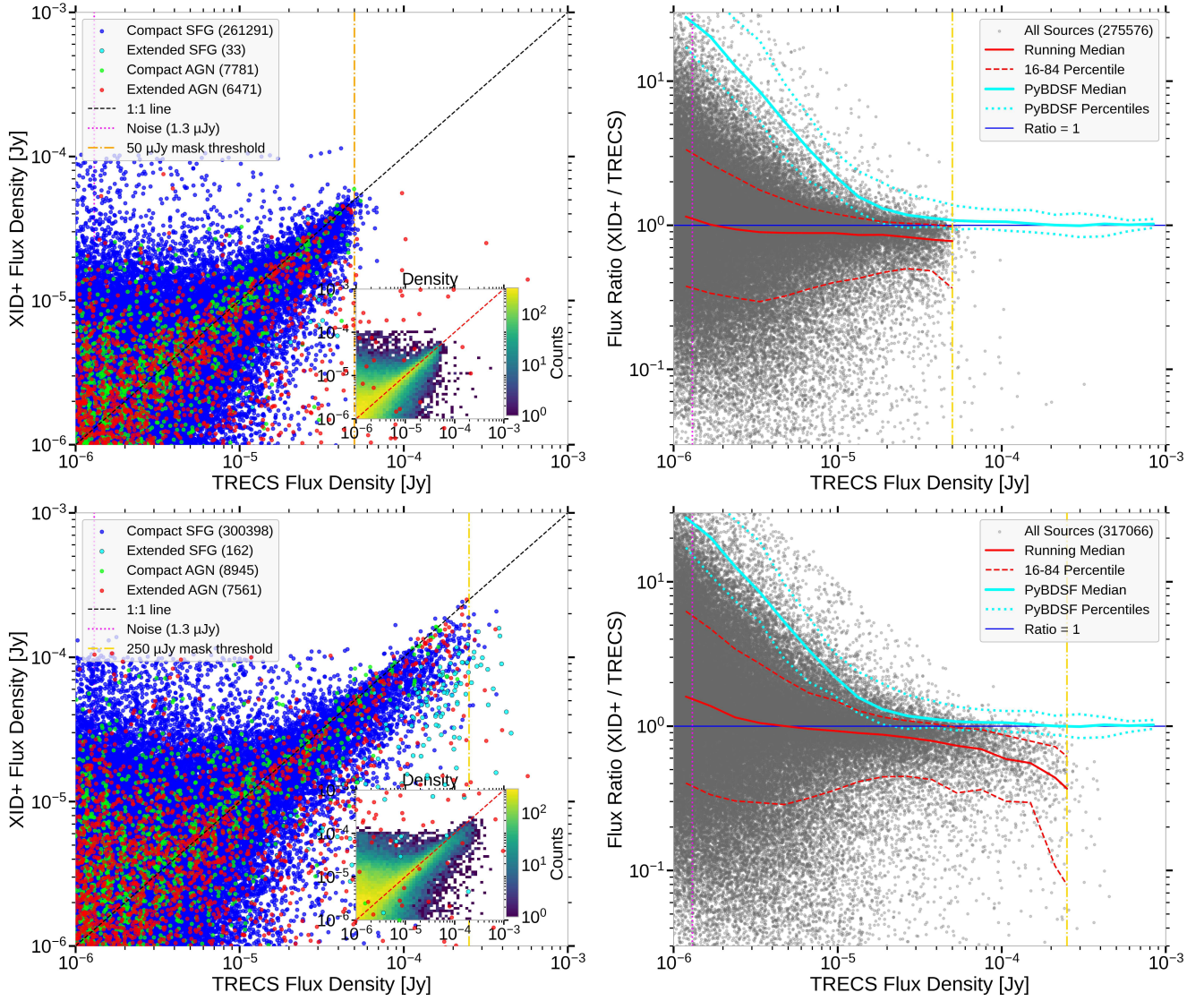


Figure B1. XID+ debinding performance using the full T-RECS prior with masks derived from the PyBDSF GAUL catalog. The panels and symbols are the same as in Figure 6. Left: Performance when masking sources brighter than $50 \mu\text{Jy}$ using the GAUL catalog. Right: Performance when masking sources brighter than $250 \mu\text{Jy}$ using the GAUL catalog. The results are qualitatively identical to the SRL-masked case shown in Figure 6, with the $50 \mu\text{Jy}$ mask yielding lower scatter.

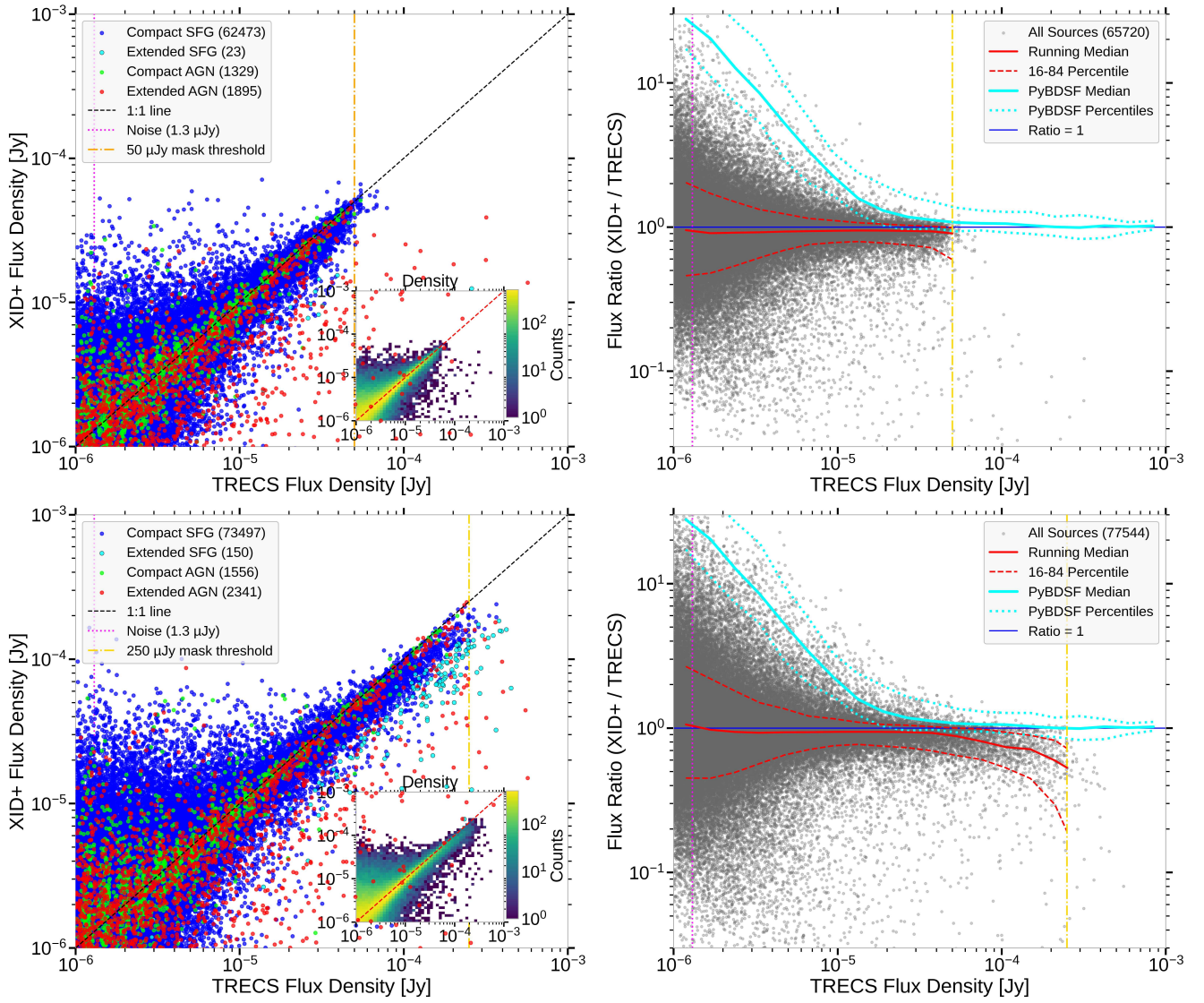


Figure B2. XID+ debrending performance using the realistic, incomplete Radio-Likely Prior with masks derived from the PyBDSF GAUL catalog. The panels and symbols are the same as in Figure 6. Left: Performance with a 50 μJy GAUL mask. Right Plot: Performance with a 250 μJy GAUL mask. As with the SRL-masked case (Figure 7), the 50 μJy mask produces the most reliable flux measurements with the tightest correlation.

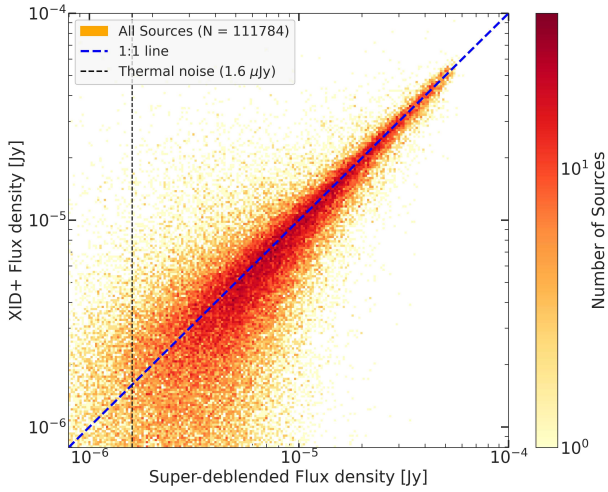


Figure C1. Comparison of XID+ deblended flux densities against the super-deblended flux densities for the unfiltered sample derived using the *Comprehensive L_{IR} Prior*.

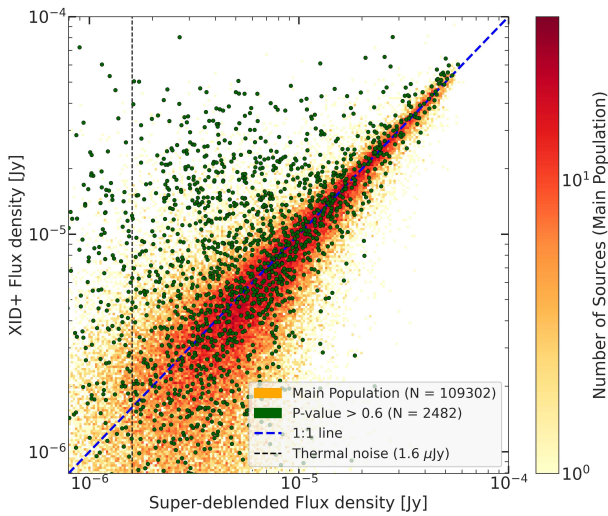


Figure C2. The same as Figure C1, but with sources having an unreliable fit (p -value > 0.6) highlighted.

Table D1. Euclidean-normalized source counts for the MIGHTEE XID+ Radio-Likely prior catalog.

Flux Bin (mJy)	Number of Sources	Source Counts ($\text{Jy}^{1.5} \text{sr}^{-1}$)	68 per cent CI Region ($\text{Jy}^{1.5} \text{sr}^{-1}$)
1.000 – 1.585	5900	0.04	[0.02, 0.04]
1.585 – 2.512	8166	0.12	[0.07, 0.11]
2.512 – 3.981	11379	0.33	[0.19, 0.31]
3.981 – 6.309	13548	0.78	[0.50, 0.74]
6.309 – 10.000	11772	1.35	[1.08, 1.45]
10.000 – 16.000	8627	1.9	[1.59, 3.02]
16.000 – 25.000	4899	2.3	[1.98, 6.18]
25.000 – 40.000	2484	2.22	[1.97, 7.99]

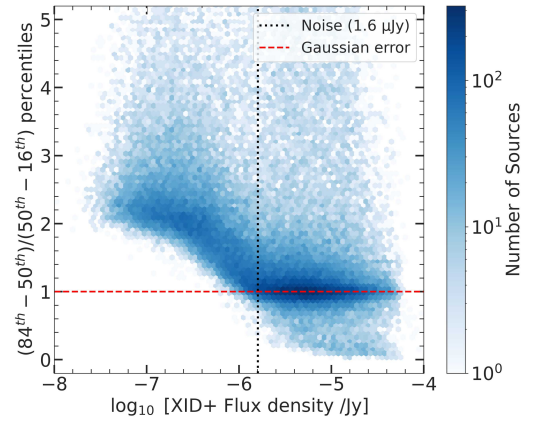


Figure C3. The ratio of the upper to lower flux density uncertainty as a function of the deblended XID+ flux for sources from the *Comprehensive L_{IR} Prior*.

Table D2. Columns contained in our XID+ deblended MIGHTEE source catalog.

Name	Unit	Description
ID	-	The COSMOS2020 ID
R.A.	-	Right Ascension from COSMOS2020
Dec.	-	Declination from COSMOS2020
Flux_med	mJy	MIGHTEE 1.3 GHz flux density (median)
Flux_MAP	mJy	MIGHTEE 1.3 GHz flux density (Marginal MAP from KDE)
Flux_Err_u	mJy	MIGHTEE 1.3 GHz flux density (84th Percentile)
Flux_Err_l	mJy	MIGHTEE 1.3 GHz flux density (16th Percentile)
bkg	mJy/Beam	Fitted Background of MIGHTEE 1.3 GHz map (median)
Rhat	-	Convergence Statistic (ideally < 1.2)
n_eff	-	Number of effective samples (ideally > 40)
P-value_res	-	Bayesian p-value residual statistic (ideally < 0.6)